

AD-A236 022



2

DTIC
ELECTE
JUN 04 1991
S D D

UNIVERSITY OF MIAMI

AN ISOPYCNIC COORDINATE NUMERICAL MODEL OF THE AGULHAS
CURRENT WITH COMPARISON TO OBSERVATIONS

By
Kevin A. Maillet

A THESIS

Submitted to the Faculty
of the University of Miami
in partial fulfillment of the requirements for
the degree of Master of Science

DISTRIBUTION STATEMENT A

Approved for public release
Distribution Unlimited

Coral Gables, Florida
December 1990

original contains color
label: ALL INFO registered
will be in black and
white

91 5 28

403

91-00651



UNIVERSITY OF MIAMI

AN ISOPYCNIC COORDINATE NUMERICAL MODEL OF THE AGULHAS
CURRENT WITH COMPARISON TO OBSERVATIONS



By
Kevin A. Maillet

A THESIS

Submitted to the Faculty
of the University of Miami
in partial fulfillment of the requirements for
the degree of Master of Science

Accession For	
NTIS CRA&I	<input checked="checked" type="checkbox"/>
DTIC TAB	<input type="checkbox"/>
Unannounced	<input type="checkbox"/>
Justification	
By	
Distribution/	
Availability Codes	
Dist	Avail and/or Special
A-1	

Coral Gables, Florida

December 1990

*Original contained color
plates: All DTIC reproductions
will be in black and
white*

UNIVERSITY OF MIAMI

A thesis submitted in partial fulfillment of
the requirements for the degree of
Master of Science

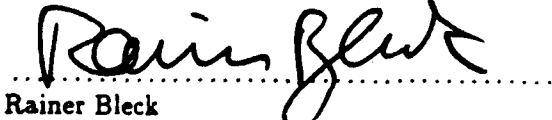
AN ISOPYCNIC COORDINATE NUMERICAL MODEL OF THE AGULHAS
CURRENT WITH COMPARISON TO OBSERVATIONS

Kevin A. Maillet

Approved:

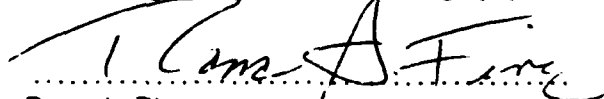


Donald B. Olson
Committee Co-Chair and Professor
Meteorology and Physical Oceanography



Rainer Bleck
Professor of Meteorology
and Physical Oceanography

.....
Douglas B. Boudra (deceased)
Committee Co-Chair and Associate Professor
Meteorology and Physical Oceanography



Rana A. Fine
Associate Professor of Marine and Atmospheric
Chemistry

.....
Pamela A. Ferguson
Dean of the Graduate School
and Associate Provost

MAILLET, KEVIN A..

(M.S., Meteorology and Physical Oceanography)

**An Isopycnic Coordinate Numerical Model of the Agulhas Current With
Comparison to Observations.**

(December 1990).

Abstract of a master's thesis at the University of Miami. Thesis supervised by Professor Donald B. Olson and Douglas B. Boudra (deceased).

No. of pages in text 71

Numerical modeling of the Agulhas Current in a limited domain begun by Boudra and Chassignet (1988) is extended. First, five experiments designed to investigate the effects of increased vertical resolution and isopycnal coordinate interface outcropping on the model retroflection and rings are described. Next, two experiments carried out in a more realistically sized basin with more realistic coastal geometry are compared with observations recently collected in the Agulhas region.

Five experiments are described to investigate increased vertical resolution and interface outcropping. They proceed from a 3-layer case to a 5-layer case with very thin upper layers. Isopycnal outcropping along the subtropical convergence and around the edge of the Indian Ocean subtropical gyre is a primary feature of three of the new experiments. In addition, some characteristics of ring formation are more realistic than in previously published experiments: e.g., formation is more frequent and is typically west or southwest of the Agulhas Bank as opposed to on the southeast side. The new experiments are generally less energetic. Energy input by the wind is pumped into the lower layers through baroclinic instability and dissipated more efficiently.

A three layer experiment and a five layer experiment are run in a larger domain configured on a Mercator projection in order to compare the results to the observations. Observations in the Agulhas region include a two year time series of velocity measurements from ten current meters moored in the Agulhas, as well as satellite sea surface height measurements of Agulhas eddies. Kinetic energy spectra from the observations south of Africa suggest an eddy shedding frequency of approximately 5 eddies per year. The models produce mean and eddy flows of similar magnitude to the observed. The solutions are in general less turbulent than the observed flow. The character of the retroflection in both experiments differs from that inferred from the observations. In the three layer model, the retroflection occurs too far up the African coast. The five layer model retroflects somewhat further down the coast.

Both models form rings that propagate too close to the coast causing the mean flow to differ from the observations. In the five layer case with thin upper layers, an inequity develops between the mean upper layer thicknesses in the Indian and Atlantic Oceans: the top layer fluid tends to become trapped in the Atlantic Ocean. This, in turn, has an impact on the dynamics of the retroflection and ring formation. The average net volume flux calculated due to this flow around Africa in the upper layer is 1.1 Sverdrups. It is concluded that, in the future, some account must be made for thermodynamic forcing, by which upper layer Atlantic Ocean water downwells and returns along intermediate isopycnals to the Indian Ocean where it then upwells back into the top layer.

Acknowledgements

As with any substantial undertaking, the completion of this work could not have been realized without the help and support of many individuals. First and foremost, I wish to acknowledge that this effort was begun by Dr. Douglas Boudra, whose untimely passing was so unfortunate and to whom I owe a great deal of thanks for getting me started in numerical modeling. I am proud to have been able to finish what he started.

I would like to thank my committee for their helpful guidance throughout the term of this project. To Dr. Rainer Bleck, who helped me get the models running; to Dr. Rana Fine, who gave me many helpful suggestions regarding the manuscript; and to Dr. Donald Olson, who took over my misguided graduate career (again) – I extend my heartfelt thanks.

To all those who made my time as a graduate student a little more enjoyable, I thank my friends. I will never forget and always appreciate the support I received from Linda Smith especially, but from all of the MPO gang. And thanks too, to my inter-departmental friends, Bill Precht, Tom Nye, the softball guys, and the whole lunch crowd. To Debbie I extend my thanks for tolerating me while I went through the rough times.

Thanks also go to Dr. Eric Chassignet, who did all he could to keep me on the right track when it was all I could do to keep moving forward. And I would like to thank the technical people who made things run a little more smoothly all the time: the RCF group of Grant, Hank, and Silvia, and Jean Carpenter, who helped me in drafting my figures.

Finally, I wish to express my gratitude to my parents, who have supported me both emotionally and financially throughout my student years. And to my uncle Jack, thanks for making me want to be a scientist.

This work was supported by the Office of Naval Research Contract No. N00014-89J-1138. Computations were carried out using the CRAY computer by remote access at the Naval Research Laboratory (NRL).

Contents

Acknowledgements	iii
List of Tables	vi
List of Figures	vii
1 Introduction	1
2 Model Description	6
2.1 Model Equations	7
2.2 Model Numerics	8
2.3 Model Basins and Boundary Conditions	9
3 Small Basin Experiments	12
3.1 Experimental Setting and Parameters	13
3.2 Experiment Characteristics	14
3.3 The Model Agulhas Rings	21
3.3.1 Three Layers (E11 and FCT1)	21
3.3.2 Four Layers (FCT2 and FCT3)	24
3.3.3 Five Layers (FCT4)	28
3.4 Summary	30
4 Large Basin Experiments	33
4.1 Introduction	33
4.1.1 Agulhas Current Observations	34
4.1.2 Experimental Design	38
4.2 Results	41
4.2.1 Experiment MERC1	41
4.2.2 Experiment FCTMERC	48
4.3 Summary	55

5 Discussion	59
5.1 Effects of increased vertical resolution	59
5.2 Comparison with observations	60
5.3 Concluding Remarks	62
A Wind Stress Application	63
References	67

List of Tables

3.1	Distinguishing parameters and some equilibrium characteristics of the experiments. The basin A.P.E. is area-averaged as is the K.E. The R_d are the baroclinic radii of deformation.	13
3.2	Typical ring characteristics among the experiments. Blanks indicate no change from the previous experiment.	21
4.1	Parameters of the two experiments described in Chapter 4. Blanks indicate no change from previous experiment.	41

List of Figures

1.1	De Ruijter's linear Agulhas current model solution	3
1.2	A calculated path of the Agulhas current from Ou and de Ruijter's model .	4
1.3	Mean streamfunction from Bouara and Chassignet's three-layer model solution	5
2.1	Geometry of the flat bottom ocean basin used in the experiments described in Chapter 3. The wind stress profile is shown at left.	11
2.2	Geometry of the flat bottom ocean basin used in the experiments described in Chapter 4. The wind stress profile is shown at left.	11
3.1	Streamfunction averaged over four years in the layer with the strongest retroflexion for experiment E11 a.), FCT1 b.), FCT2 c.), FCT3 d.), and FCT4 e.). The contour interval is 5 Sv.	15
3.2	Bottom layer streamfunction averaged over four years for experiment E11 a.), FCT1 b.), FCT2 c.), FCT3 d.), and FCT4 e.). The contour interval is 5 Sv.	19
3.3	The layer 1 velocity and thickness fields averaged over the final 1825 days of the 3650 day experiments E11 a.) and FCT1 b.).	23
3.4	Typical layer 1 velocity and thickness fields a. a ring is being formed in experiments E11 a.) and FCT1 b.). The contours and barbs are as in Fig. 3.3.	25
3.5	Typical layer 1 a.) and layer 2 b.) velocity and interface depth fields for experiment FCT2. The contours and barbs are as in Fig. 3.3. Grid points represented by dots indicate where the layer below is outcropped.	26
3.6	Instantaneous layer 1 a.) and layer 2 b.) velocity and interface depth fields for experiment FCT3 very close to an event of ring cutoff. The contours and barbs are as in Fig. 3.3 and the grid points represented by dots indicate where the layer below has outcropped.	29

3.7	Instantaneous layer 3 flow patterns and interface 3 depth fields 25 days apart in FCT4. Note the intrusion of subpolar fluid associated with development of two rings. The contours and barbs are as in Fig. 3.3 and the grid points represented by dots indicate where the layer below has outcropped.	31
4.1	Mean current vectors computed from a two year velocity time series. Overlaid is a path of the Agulhas Current derived by navigating along the intersection of the 15° isotherm and the 200 m depth contour.	35
4.2	Values of mean eddy kinetic energy at the current meter moorings in a.) the upper ocean (200 m) and b.) the deep ocean (5000 m).	36
4.3	Kinetic energy spectra in the upper ocean from moorings a.) 838 and b.) 839 (units are in $10^5 cm^4 sec^{-4}$) and c.) squared coherence (confidence interval is 95 %).	38
4.4	Kinetic energy spectra from mooring 838 a.) upper ocean, b.) deep ocean (units are in $10^5 cm^4 sec^{-4}$) and c.) squared coherence (confidence interval is 95 %).	39
4.5	As in Fig. 4.4 for mooring 839.	39
4.6	RMS variability of the geostrophic velocity for the South Atlantic/Agulhas region during the period November 1986 to November 1987 as measured by the Geosat altimeter (from Gordon and Haxby, 1989).	40
4.7	Trajectories of seven selected eddies, labelled A through G as measured by the Geosat altimeter (from Gordon and Haxby, 1989). The track labeled M is a typical eddy track from the models described in this Chapter.	40
4.8	Mean flow vectors from current meter data and experiment MERC1. Heavy solid arrows depict current meter data. Heavy dashed arrows depict model data at the current meter location. Small arrows are model velocities. Contour lines indicate model mean interface depth in meters.	42
4.9	Mean eddy kinetic energy over the final four years of experiment MERC1 in a.) the upper layer and b.) the bottom layer.	43
4.10	A series of instantaneous flow field and interface depth contours from experiment MERC1.	44
4.11	Kinetic energy spectra in layer 1 of exp. MERC1 from moorings a.) 5 and b.) 6 (units are in $10^5 cm^4 sec^{-4}$) and c.) squared coherence (confidence interval is 95 %).	46

4.12	Kinetic energy spectra from exp. MERC1 mooring 5 a.) layer 1, b.) layer 3 (units are in $10^5 cm^4 sec^{-4}$) and c.) squared coherence (confidence interval is 95 %).	47
4.13	As in Figure 4.12 for mooring 6.	47
4.14	Eddy tracks during the final two years of experiment MERC1. Crosses indi- cate the location of moorings 5 and 6.	48
4.15	Mean flow vectors from current meter data and experiment FCTMERC. Heavy solid arrows depict current meter data. Heavy dashed arrows depict model data at the current meter location. Small arrows are model velocities. Contour lines indicate model mean interface depth in meters.	49
4.16	A series of instantaneous flow field and interface depth contours from exper- iment FCTMERC.	50
4.17	Mean eddy kinetic energy over the final four years of experiment FCTMERC in a.) the upper layer and b.) the bottom layer.	51
4.18	Mean layer thickness in entire domain for a.) experiment MERC1 and b.) experiment FCTMERC. Units are in meters.	53
4.19	Kinetic energy spectra in layer 1 of exp. FCTMERC from moorings a.) 5 and b.) 6 (units are in $10^5 cm^4 sec^{-4}$) and c.) squared coherence (confidence interval is 95 %).	55
4.20	Kinetic energy spectra from exp. FCTMERC mooring 5 a.) layer 1, b.) layer 5 (units are in $10^5 cm^4 sec^{-4}$) and c.) squared coherence (confidence interval is 95 %).	56
4.21	As in Figure 4.20 for mooring 6.	56
4.22	Eddy tracks during the final two years of experiment FCTMERC. Crosses indicate the location of moorings 5 and 6.	57
A.1	a.) Initial configuration for a three layer model. b.) Possible configuration of model after integration has proceeded for some time. Wind stress profile is at left. (Figure not to scale.	64

Chapter 1

Introduction

Numerical models have become powerful tools for understanding physical processes in the world oceans. The first numerical ocean models were aimed at identifying these processes and as such their domains bore little resemblance to realistic ocean basins. Bryan and Cox (1968) developed a nonlinear, baroclinic ocean model based on the full equations of motion forced by both wind and thermohaline effects and formulated on an idealized basin. Their model yielded one of the first baroclinic, numerical representations of large scale ocean circulation features including western boundary currents and equatorial circulations. Holland and Lin (1975) developed a primitive equation ocean model formulated in a rectangular domain with high horizontal resolution. Their model led to the realization of the importance of mesoscale eddies to the general circulation of the ocean. Later, Holland (1978) used a model based on the quasi-geostrophic approximation to the full equations of motion to further investigate the role of mesoscale eddies.

With the advent of powerful supercomputers, the ability to construct models in domains which better represent actual ocean basins and have mesoscale horizontal resolution has been realized. Supported by this increased computing power, numerical ocean models have evolved towards realistic simulations of specific ocean regions and even global ocean circulation. Hurlburt and Thompson (1980) have modeled the Gulf of Mexico and Thompson and Schmitz (1989) the North Atlantic Ocean using a high resolution primitive equation model. Bryan and Cox's model (1968) has been expanded into a global ocean simulation by Semtner and Chervin (1988).

With the evolution of numerical models from process study tools to actual ocean simulations comes the need to verify these simulations through comparisons of model results with observations of the real ocean. At the very least, a useful ocean model must simulate the large scale features of the circulation and ideally, with high resolution models,

mesoscale variability should be reproduced in a manner somewhat resembling the real ocean. The comparison between models and observations assumes a particularly important role in the context of global change. We must document our environment through extensive measurement in order that we may detect changes in the natural system as well as verify, or refute, changes predicted by our modeling efforts. It is only through constant and consistent comparison of model results with ocean measurements that we can hope to improve the ability of the models to simulate real world conditions. This work represents such a comparison in which a regional numerical ocean model of the Agulhas Current is compared to observations collected in the Agulhas region south of the African continent.

The Agulhas Current system is one of the most dynamically interesting current systems in the world. The Agulhas is the major western boundary current in the South Indian Ocean. It is unique in that the African coast terminates before the current reaches the zero in the wind stress curl in the Indian Ocean basin. Thus, the Agulhas is faced with the possibility of clinging to the African coast and entering the South Atlantic Ocean or separating from the coast and turning back into the Indian Ocean basin. Observations show that the major portion of the Agulhas chooses the latter route, separating from the coast at approximately 36° S and "retroreflecting" into the Indian Ocean. This situation however, does leave open the possibility of interocean transfer of warm, salty Indian Ocean thermocline water into the cooler, fresher South Atlantic. This transfer could be the result of changes in the external forcing of the Agulhas, where variations in wind or thermal driving would allow more or less direct "leakage" of Agulhas water around Africa's tip, or the result of internal fluid dynamics effects. Indeed, observations and modeling studies have suggested that occasionally, upon retroreflecting, the Agulhas pinches itself off, forming a lens of warm salty water, commonly referred to as an Agulhas ring. Once separated from the Agulhas proper, these rings essentially become isolated eddies in the large scale flow field and as such, usually drift westward and eventually northwestward into the Atlantic Ocean basin, carrying with them their characteristic warm temperature signal, higher salinity, and high potential vorticity. These rings eventually lose their anomalous temperature signature at the surface due to the intense heat flux from the sea surface in the eastern South Atlantic (Walker and Mey, 1988). However, evidence of their subsurface properties as well as their sea surface height signal has been observed well into the Atlantic basin, away from the Agulhas region (Olson *et al.*, 1990; Gordon and Haxby, 1989).

The effects of the transfer of Indian Ocean water into the South Atlantic in the Agulhas region have been the subject of much theory. Gordon (1986) believes that the introduction of warm Indian Ocean thermocline water into the Atlantic balances the export of North

Atlantic deep water which is formed in high latitudes of the Northern Hemisphere and subsequently flows down the North American coast as a deep western boundary current. Olson et al. (1988) present evidence that suggest that Agulhas rings undergo local convective events as a result of air-sea interaction in the South Atlantic. There is speculation that these events may be partially responsible for the ventilation of the South Atlantic thermocline waters (Fine et al., 1985).

Previous studies of the Agulhas retroflection have been both analytical and numerical. Lutjeharms and van Ballegooyen (1984) studied the topographic control of a free jet as applied to the Agulhas current. They found that small variations in bottom velocity of the model produced great changes in the path of the current after separation from the African coast. They also found that the volume transport of the jet was a controlling factor in whether the current rounded the African coast into the Atlantic or retroflected somewhere up the coast.

De Ruijter (1982) used a Munk-type model which includes the β -effect and lateral friction to represent the South Atlantic-Indian Ocean region. He found that this linear model was incapable of producing a retroflection. Figure 1.1 shows that this model produced one giant gyre system with a western boundary current at the extreme western wall, corresponding to the Brazil current system, and a western boundary current along the eastern African coast, the model Agulhas current, with a small recirculation just to the west of Africa.

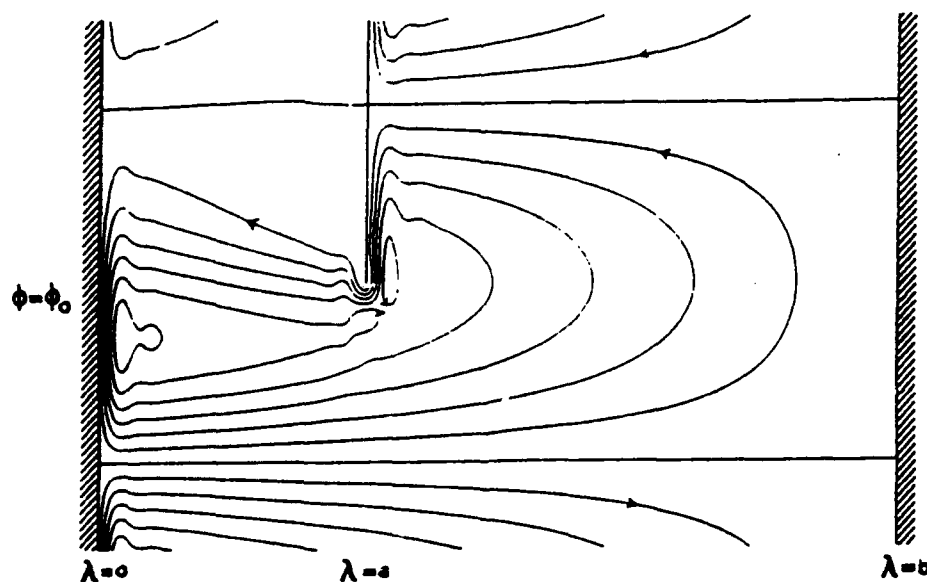


Figure 1.1: De Ruijter's linear Agulhas current model solution

Ou and de Ruijter (1986) applied an inertial boundary current separation model to the

Agulhas. This 1-1/2 layer model included inertia, the β -effect, and coastline curvature. The model Agulhas separated from the coast when the motionless lower layer outcropped at the sea surface. The Agulhas was seen to undergo a retroflection subsequent to separation (Figure 1.2). The position of separation and retroflection were strongly influenced by

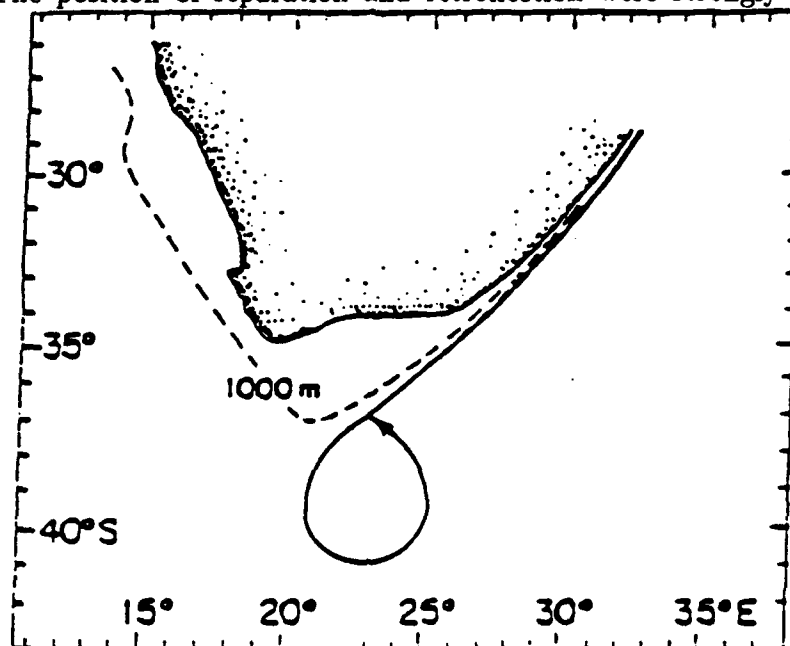


Figure 1.2: A calculated path of the Agulhas current from Ou and de Ruijter's model

coastline curvature, the current separating sooner for a convex South Africa than for a straight coastline. Volume transport of the current was also an important factor in the separation and retroflection positions.

De Ruijter and Boudra (1985) and Boudra and de Ruijter (1986) carried out numerical experiments to investigate the Agulhas retroflection using the Bleck and Boudra (1981) quasi-isopycnic coordinate ocean model. This work was expanded by Boudra and Chassignet (1988) and Chassignet and Boudra (1988). Boudra and Chassignet (1988) proceeded systematically from a linear, one-layer version of the model to a fully nonlinear, three layer version in which African coastal geometry is represented as a triangular shape. The Agulhas retroflection is explained in terms of a change in the vorticity balance of the current at the tip of the African continent. With a no-slip African boundary condition, the increase of planetary vorticity as the current separates from the coast causes the anticyclonic turning of the Agulhas back towards the Indian Ocean. It was found that the stretching term plays a major role as well in the retroflection as fluid attempting to leak around the tip of Africa experiences a torque due to the potential vorticity contrast between the Agulhas region and the South Atlantic. Figure 1.3 shows the retroflection in their three layer, triangular experiment. Chassignet and Boudra (1988) examined the energetics of the model Agulhas

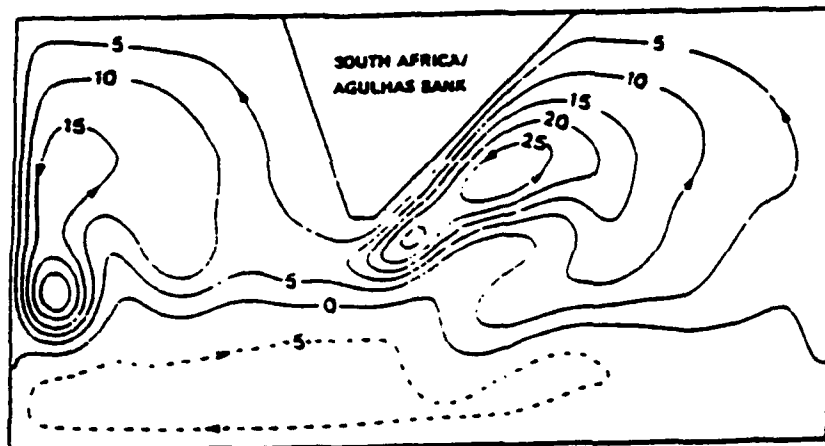


Figure 1.3: Mean streamfunction from Boudra and Chassignet's three-layer model solution and the dynamics of ring formation events.

This work will describe the most recent extension of the work begun by Boudra and de Ruijter (1986) and extended by Boudra and Chassignet (1988) to include multi-layer models and a more realistic coastal configuration. It will be organized as follows: Chapter 2 will describe the models used and the experimental setting. Chapter 3 will discuss some preliminary experiments which investigate the effects of vertical resolution and stratification on the retroflection. Chapter 4 will compare the results of two experiments in a more realistic domain with observations gathered in the Agulhas region, and Chapter 5 will summarize the results and discuss their implications.

Chapter 2

Model Description

The models used in this study are

- the Bleck and Boudra (1981) primitive equation, quasi-isopycnic coordinate ocean model
- the Bleck and Boudra (1986) pure isopycnic coordinate model

These models are formulated in a similar manner, but differ in that the pure isopycnic model allows surface outcropping of the coordinate interfaces. As such, the models have somewhat different conservative properties which result from the existence of layers of zero thickness and the corresponding prohibition of division by layer thickness.

Briefly described, the isopycnic coordinate numerical ocean model can be thought of as a stack of shallow fluid layers, each governed by a set of equations resembling the shallow water equations. The layers interact through hydrostatically transmitted pressure forces at the layer interfaces. The advantages to a model configured in such a coordinate system are as follows:

1. In contrast to models formulated in an Eulerian vertical coordinate, a model with density as the vertical coordinate gains vertical resolution wherever needed by the dynamical migration of grid points into regions of strongest density contrast. This provides the model with optimal resolution of baroclinic structures.
2. Solving the prognostic equations along isopycnic surfaces is consistent with the belief that in the ocean, mixing is along rather than across isopycnal surfaces (Montgomery, 1938; Redi, 1982).
3. The isopycnic coordinate finite difference primitive equations can be formulated so as to conserve potential vorticity and potential enstrophy in the absence of diabatic

forcing, unlike the finite difference equations formed in Eulerian coordinates.

These advantages may be overshadowed by the numerical difficulties encountered when coordinate surfaces migrate towards and touch each other or the sea surface in baroclinic regions. In fact, the finite difference equations lose their quadratic conservative property in regions where isopycnals merge or outcrop. The Bleck and Boudra (1981) model avoids such coordinate surface intersections by resorting to an Eulerian system when layer thickness is predicted to violate some minimum thickness condition. The pure isopycnic model described by Bleck and Boudra (1986) must take into account the existence of massless layers in the domain. This particular model uses the Flux Corrected Transport (FCT) algorithm (Zalesak, 1979) for computing mass flux divergences to deal with this requirement.

The models are configured on two basins. Experiments designed to examine the sensitivity of the retroflection to changes in vertical resolution and upper ocean static stability were first performed in the basin used by Boudra and Chassignet (1988). A larger, more realistic domain was then designed to perform experiments to compare with observations.

2.1 Model Equations

The primitive equation, isopycnic coordinate model may be viewed as a stack of shallow fluid layers, each consisting of a momentum and a continuity equation:

$$\frac{\partial \vec{v}}{\partial t} + \frac{1}{2} \nabla_{\rho} \vec{v}^2 + \eta \hat{k} \times \vec{v} = -\nabla_{\rho} M + \alpha \frac{\partial \vec{\tau}}{\partial z} + A(\delta_{\rho} p)^{-1} \nabla_{\rho} \cdot \delta_{\rho} p \nabla_{\rho} \vec{v} - \sigma \vec{v}, \quad (2.1)$$

$$\frac{\partial}{\partial t}(\delta_{\rho} p) + \nabla_{\rho} \cdot (\vec{v} \delta_{\rho} p) = 0, \quad (2.2)$$

where $\eta = \xi + f$ is the absolute vorticity ($\xi = v_x - u_y$); $M = gz + p\alpha$ is the Montgomery potential; the "layer pressure-thickness", $\delta_{\rho} p$, is the thickness of a layer of constant density, ρ ; the specific volume, $\alpha = \rho^{-1}$; τ is the wind stress; A is the lateral viscosity; and the bottom drag coefficient, σ , is zero except in the bottom layer. The subscript ρ indicates derivatives on surfaces of constant density. These shallow water layers communicate vertically through hydrostatically transmitted pressure forces, according to the hydrostatic equation:

$$\frac{\partial M}{\partial \alpha} = p. \quad (2.3)$$

The quasi-isopycnic model consists, in addition, of a thermodynamic equation, which is of consequence in regions of a layer where density varies. As described in Bleck and Boudra (1981) this occurs when water from a lower layer is transferred to the layer above whenever a

coordinate surface rises to within a minimum distance from the surface above it. Thus, the model loses its isopycnic character in regions where coordinate surface outcropping would otherwise occur. Neglecting diabatic processes, compressibility effects, and temperature and salinity conservation, this thermodynamic equation has the form

$$\frac{\partial \alpha}{\partial t} + \bar{v} \cdot \nabla_s \alpha + \left(\bar{s} \frac{\partial p}{\partial s} \right) \frac{\partial \alpha}{\partial p} - A \left(\frac{\partial p}{\partial s} \right)^{-1} \nabla_s \cdot \left(\frac{\partial p}{\partial s} \nabla_s \alpha \right) = 0. \quad (2.4)$$

The horizontal derivatives are with respect to the generalized coordinate s rather than density *per se*. The horizontal pressure force is expressed in terms of both geopotential and pressure gradients along coordinate interfaces, and the momentum and continuity equations also include vertical advection terms. For details on how the vertical motion \bar{s} is computed, the reader is referred to Bleck and Boudra (1981).

2.2 Model Numerics

In two primary ways, the numerical integration of the pure- and quasi-isopycnic models differs. First, in the quasi-isopycnic model, the continuity equation is formulated in 2nd-order centered finite difference form and integrated forward with leap frog. In the pure-isopycnic model, mass fluxes into and out of grid boxes are initially estimated using 1st-order, upstream approximations. Those fluxes are then corrected by means of *anti-diffusive* fluxes determined by the difference between the first order and some higher order¹ approximation—that is, assuming full incorporation of the anti-diffusive fluxes would yield non-negative layer thickness. If the latter condition is not satisfied, the low and high order approximations are blended, so that negative thickness is avoided. For more detail, see Bleck and Boudra (1986).

The second difference in the model numerical integrations is related to the allowance of zero layer thickness in the pure-isopycnic model. Bleck and Boudra (1981) formulated the finite differences of the third term on the left of (1) such that the nonlinear terms in the quasi-isopycnic model conserve potential vorticity and potential enstrophy, provided the coordinate surfaces remain isentropic (isopycnic). In the strict sense, this is not possible in the pure-isopycnic model because of a division by layer thickness, which may vanish. It is likely that some provision can be made for a conservative formulation in regions where layer thickness is bounded away from zero and a smooth transition to a non-conservative operator in outcropping zones. Such has not been attempted in the experiments to be described here, however, and instead a less conservative formulation has been used. On the other hand,

¹In the present case, 2nd order.

the outcome of the two formulations must converge as grid spacing tends to zero—that is, as the numerical solutions tend to the exact solution. Boudra and Chassignet (1988) found that the conservation terms in the quasi-isopycnic model spelled the difference between a strong (with conservation) and a weaker (without conservation) retroflection when using 40 km grid spacing. In the specific case of the 20 km horizontal resolution experiment E11, the ten-year integration has since been extended three years, first with the conservative and then with the less conservative formulation. The mean flow patterns and the mean and eddy energy fields of these two extensions have very small differences. It is felt, therefore, that the use of 20 km resolution here is sufficient to avoid large errors which might result from lack of exact potential vorticity and potential enstrophy conservation.

Since ours is a primitive equation model, the solution to the model equations includes high frequency gravity waves as well as low frequency rotational modes. Our main interests are in the lower frequency waves, so we can filter out the unwanted external gravity waves from the model solution. A rigid lid approximation is used in the model to facilitate this task. This approximation allows the use of a larger time step than would be possible if external gravity waves were present. The rigid lid approximation is implemented by removing the divergent component from the vertically integrated mass flux field after each time step.

2.3 Model Basins and Boundary Conditions

The experiments described in the first part of this work are configured on the basin depicted in Figure 2.1. The dimensions are approximately three times smaller than those of the South Atlantic/Indian Ocean, but provide an economically convenient domain size for the study of retroflection dynamics. The characteristics of this domain have been discussed by Boudra and Chassignet (1988).

In order to perform model experiments which could be compared to ocean observations, a larger, more realistic domain was used. This domain is illustrated in Figure 2.2. This domain is configured on a Mercator projection to account for the sphericity of the earth, and is bounded approximately by 25° S and 50° S latitude and by 2° E and 60° E longitude. The 1000 *m* isobath is used to represent the Agulhas Bank shelf break and the model has a flat bottom. The total basin size is approximately 5000 *km* × 2500 *km* which represents a four-fold increase in size over the previous domain.

For the large basin model, the Coriolis parameter varies as $f = 2\Omega \sin\phi$, where Ω is the angular velocity of the earth and ϕ is latitude. The model is wind forced and an

approximation of the zonal wind stress, based on the Hellerman and Rosenstein (1983) data has been incorporated. The latitudes of the zero and maximum of the stress curl have been approximately preserved from their data. The stress amplitude of 2.5 dyn cm^{-2} has been scaled so as to support $50 \times 10^6 \text{ m}^3 \text{ s}^{-1}$ (Sv.) of vertically integrated Sverdrup transport at the tip of South Africa. The application of the wind stress is described in detail in Appendix A. Briefly, the wind stress is applied as a body force to any layer which exists within a specified maximum wind forcing depth. Specifically, for the quasi-isopycnic model, the maximum wind forcing depth is 100 m. For the pure-isopycnic model, wind stress is applied to any layer existing within 20 m of the surface. This change is made in order to encourage isopycnal outcropping in the pure-isopycnic model, since the tendency for outcropping is reduced when layers below the first begin to receive wind forcing. This is because when layer two receives wind input, the resulting layer two velocities decrease the vertical shear and hence the isopycnal tilt between the layers.

Lateral boundary conditions for both models are no-slip on the meridional boundaries, free-slip on the zonal boundaries, and no-slip on the African coast.

The resulting flow patterns yield counterclockwise subtropical gyres east and west of South Africa, an elongated subpolar gyre near the southern boundary, and a region southward from Africa's tip to the latitude of wind curl zero where exchange may occur between the two subtropical gyres, depending on the strength of the model Agulhas retroflection. The northern branch of the subpolar gyre provides an eastward drift along a frontal-type feature with which the model Agulhas may interact, much as the real Agulhas Current system interacts with the northern edge of the Antarctic Circumpolar Current (ACC).

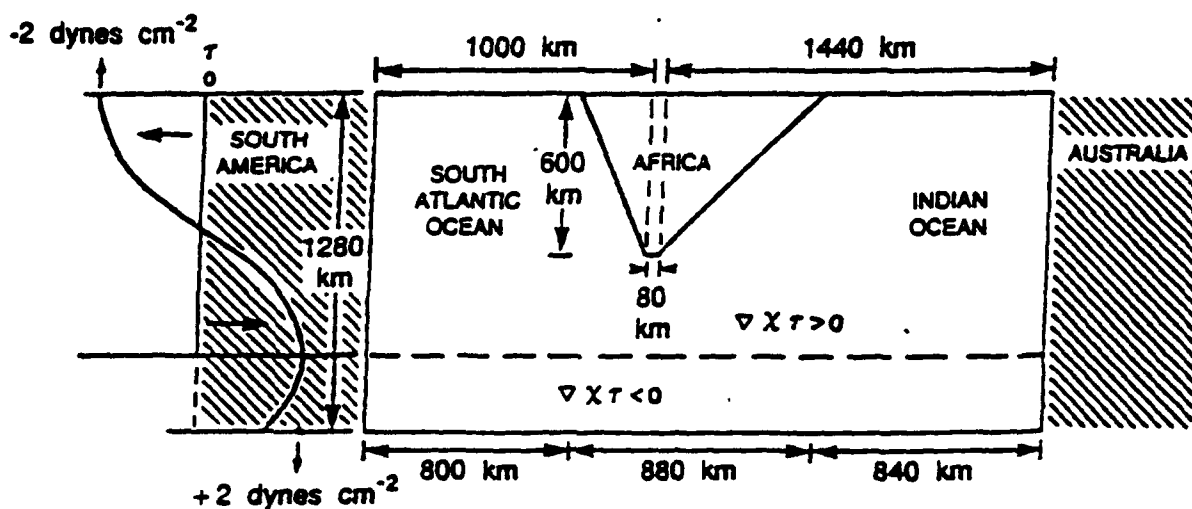


Figure 2.1: Geometry of the flat bottom ocean basin used in the experiments described in Chapter 3. The wind stress profile is shown at left.

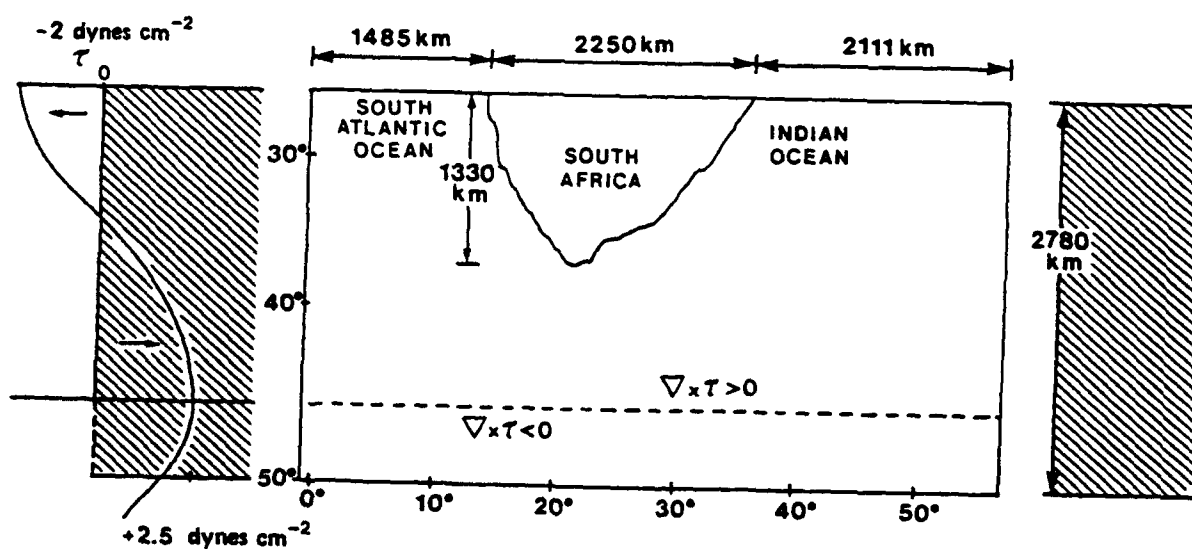


Figure 2.2: Geometry of the flat bottom ocean basin used in the experiments described in Chapter 4. The wind stress profile is shown at left.

Chapter 3

Small Basin Experiments

In this chapter we describe a first step in developing a realistic South Atlantic/Indian Ocean model and, at the same time, examine the sensitivity of the model retroflection and ring formation to upper ocean stratification and isopycnal outcropping. In some of the previous 3-layer experiments, substantial variation in isopycnal interface depth was allowed. In the high Rossby number experiments, the uppermost interface was typically 300-350 m shallower on the retroflection edge than in its center. However, the mean upper layer thickness was great enough that isopycnal outcropping occurred only in the southwestern interior of the subpolar gyre. As is the case along most separated western boundary currents of the world ocean, isopycnal outcropping around the edge of the Agulhas retroflection and Agulhas rings is pronounced (Gordon, 1985). In fact, several theoretical models of boundary current separation require the pycnocline/thermocline to surface (Charney, 1955; Parsons, 1969; Veronis, 1973; Moore and Niiler, 1974; Ou and de Ruijter, 1986) at which point the current, isolated above the thermocline, must separate. Isopycnal layered numerical models which solve the primitive equations as initial/boundary value problems over a 3-dimensional grid volume, have traditionally been hampered from allowing such interface surfacing because of numerical difficulties encountered when layer thickness is allowed to shrink to zero. This difficulty was overcome through the use of the Flux Corrected Transport algorithm as described in Chapter 2. Within this framework, coordinate layers are allowed to collapse at the upper or lower boundary (and even in the interior) in a numerically trouble-free fashion.

3.1 Experimental Setting and Parameters

The distinguishing parameters and some equilibrium characteristics of the experiments to be discussed here are given in Table 3.1. The lateral viscosity is $A = 330 \text{ m}^2 \text{ s}^{-1}$ and bottom drag coefficient $\sigma = 1 \times 10^{-7} \text{ s}^{-1}$ for all the experiments.

Exp.	Number of layers	Thickness of the layers (db)	g' ($m\ s^{-2}$)	R_d (km)	Mean Total A.P.E. $10^4\ J\ m^{-2}$	Mean Total K.E. $10^4\ J\ m^{-2}$	Mean Retroreflection Character
E11	3	300	0.02	29	13.0	1.95	Quite strong in layer one. Slightly weaker in layer two.
		900	0.005	18			
		3800					
FCT1	3	300	0.01	40	10.2	1.6	Moderately strong in layers one and two.
		900	0.015	16			
		3800					
FCT2	4	150	0.006	40	10.9	0.9	Rather weak in layers one and two. Stronger in layer three.
		150	0.004	12			
		900	0.015	6			
		3800					
FCT3	4	75	0.003	42	8.9	0.95	None in layer one. Weak in layer two. Moderately strong in layer 3.
		175	0.005	11			
		950	0.017	4			
		3800					
FCT4	5	75	0.003	40	9.05	0.82	None in layer one. Very weak in layers 2 and 3. Moderately strong in layer 4.
		75	0.003	10			
		100	0.003	4			
		950	0.016	2			
		3800					
For all experiments, $\Delta x = 20\ km.$							

Table 3.1: Distinguishing parameters and some equilibrium characteristics of the experiments. The basin A.P.E. is area-averaged as is the K.E. The R_d are the baroclinic radii of deformation.

In the fifth column of Table 3.1 are the baroclinic radii of deformation R_d corresponding to the basic stratification for each experiment, computed following Lighthill (1969). These R_d correspond to the N baroclinic modes of the system, where N is the number of layers minus one. They only give a rough indication of what the R_d are at any point within the domain after the experiments reach equilibrium. It may be noted, however, especially for experiments FCT2, FCT3, and FCT4, that resolution of the first mode is improved over that of E11, but the higher modes are very poorly resolved by the grid spacing. This results primarily from the decision to decrease the upper ocean reduced gravity (g'), and strengthen the g' across the lowest interface in order to encourage interface outcropping as a first-order priority. Adequate resolution of the higher modes would in any case be difficult with 20 km grid spacing. Five and ten kilometer resolution experiments are not currently

economically feasible. At the same time, we recognize that increasing the number of vertical modes without also increasing horizontal resolution is open to question. However, it is clear that the low order modes will be simulated correctly although the higher order modes will not.

3.2 Experiment Characteristics

The following section discusses these experiments in terms of the effect of varying static stability and vertical resolution on Agulhas rings; that is, how and where the rings form and their subsequent behavior. To set the stage for this discussion, it is first appropriate to make some general comments concerning the equilibrium characteristics of the experiments.

From the right portion of Table 3.1, we note that the equilibrium energy levels decrease first as the upper ocean static stability is reduced and then as more coordinate layers are added in the upper 300 db with very little difference between the last two experiments. An energy decrease as upper ocean resolution is increased is in contrast to the result obtained by Boudra and de Ruijter (1986) and analyzed by Boudra and Chassignet (1988) and Chassignet and Boudra (1988), where the number of layers was first increased from 2 to 3 and then the mean thickness of the top layer was reduced from 600 db to 300 db for rectangular Africa experiments. In each case, the mean total potential and kinetic energies increased. Also, however, the largest layer interface g' remained associated with the uppermost layer interface, 0.02 m s^{-2} as opposed to a lower interface g' of 0.005 m s^{-2} in the 3-layer cases. Here, this distribution is first changed to upper and lower g' 's of 0.01 and 0.015 m s^{-2} , respectively, and then as more layers are introduced near the top, correspondingly weaker g' 's are attached to the interfaces, so that the equivalent upper ocean g' is still $\sim 0.01 \text{ m s}^{-2}$. The associated energy trends, then, suggest that as static stability is reduced and vertical resolution increased, more efficient means are developed for dissipating the energy input by the wind.

Further, relating columns 4 and 8 in the Table, we find that the strongest retroflection, i.e. the largest volume of fluid returned to the Indian Ocean basin relative to the amount reaching the African tip, is generally located within the layer which has the largest g' at its base. For E11 this is layer one, but for FCT2, FCT3, and FCT4 it is the layer second from the bottom. Figure 3.1 shows the streamfunction, averaged over four years of each experiment, in the layer having the strongest retroflection. In their vorticity balance analysis, BC showed that the model retroflection strength is associated with the magnitude of the planetary vorticity advection and stretching terms as the current separates. Large

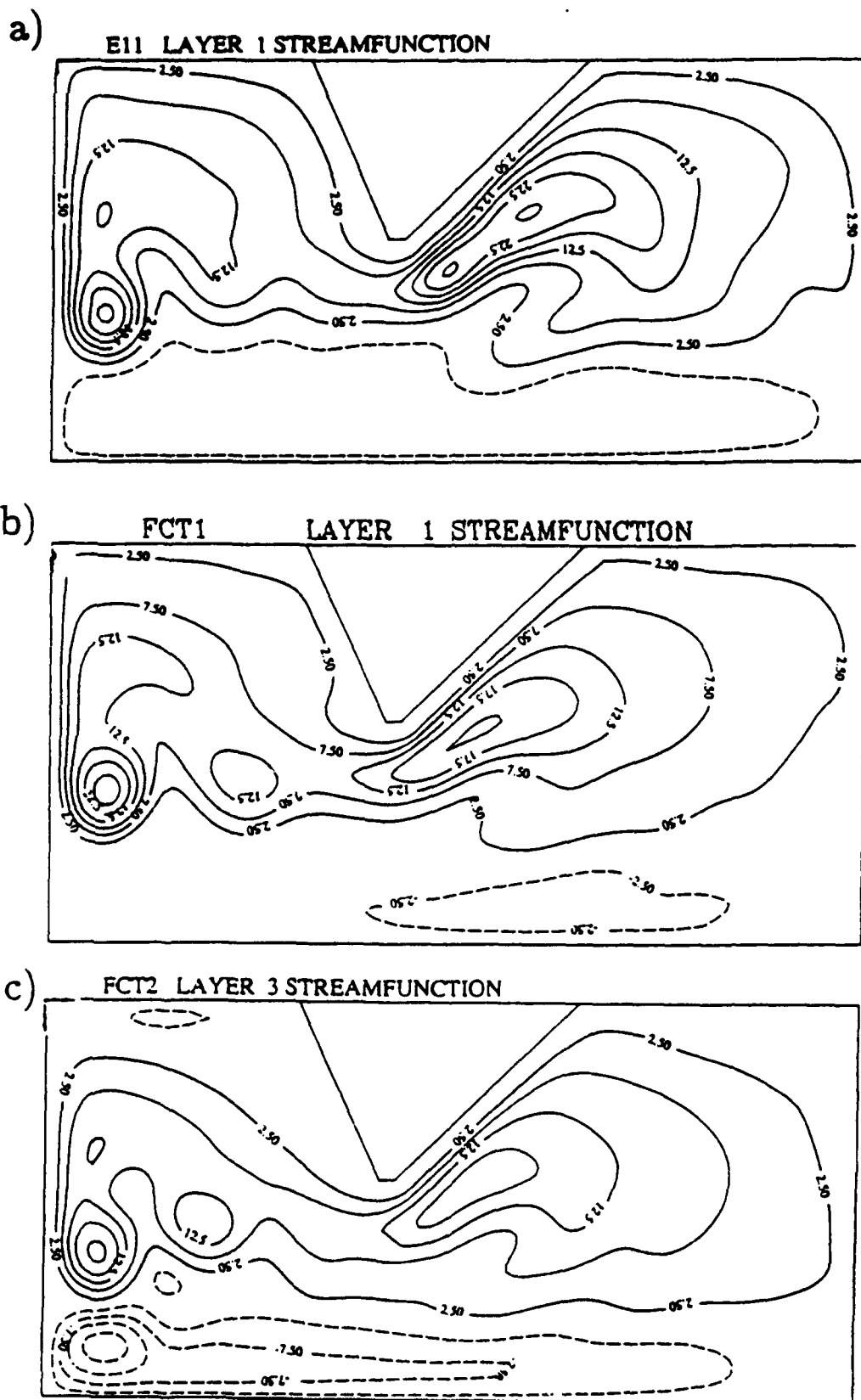


Figure 3.1: Streamfunction averaged over four years in the layer with the strongest retroflection for experiment E11 a.), FCT1 b.), FCT2 c.), FCT3 d.), and FCT4 e.). The contour interval is 5 Sv.

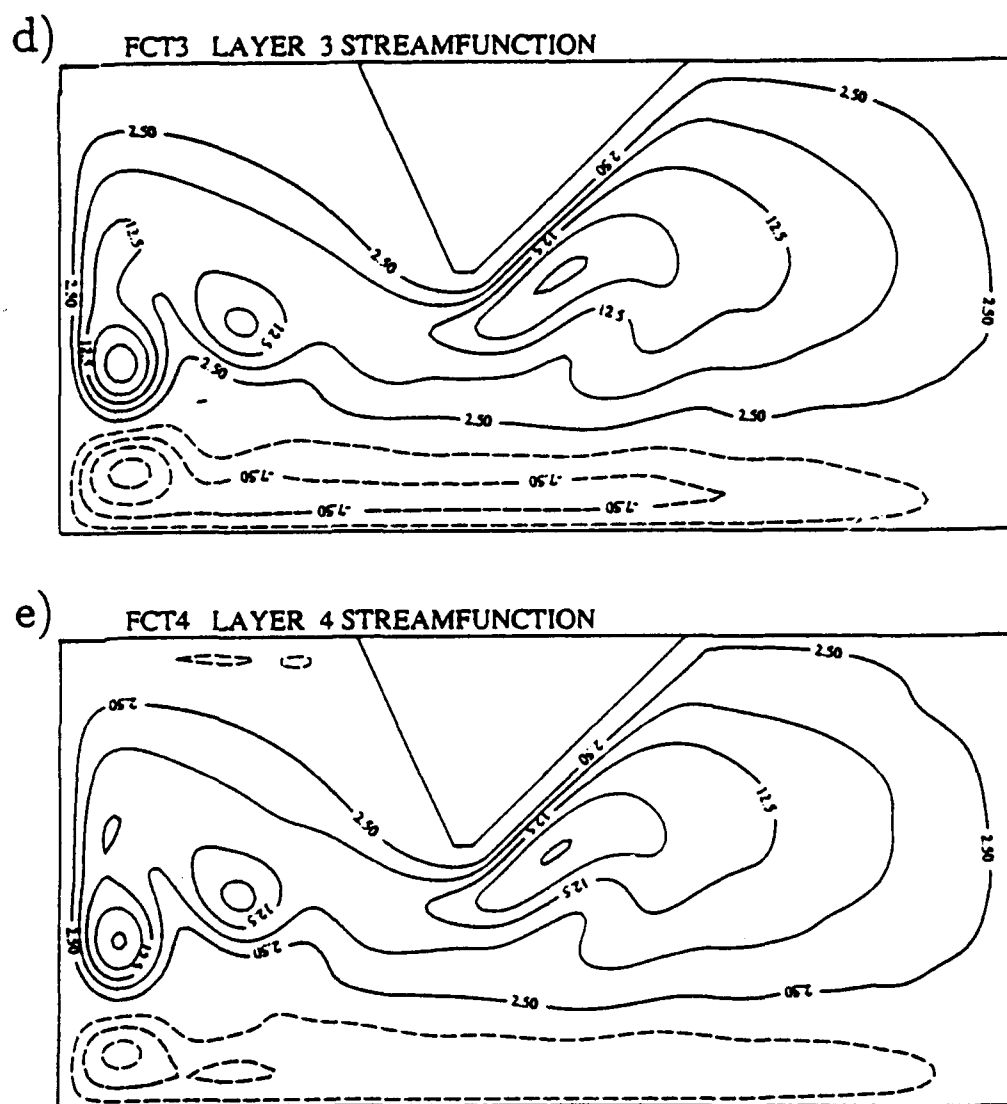


Figure 3.1 cont.

values of these terms are favored by a coherent, strong Agulhas reaching Africa's tip. In the first case, it is the southward component of motion which induces positive curvature. In the second case, it is the mean potential vorticity contrast between the southwest Indian and southeast South Atlantic Oceans which exerts a torque on fluid attempting to escape westward. In the above experiments, it seems that maintenance of such a coherent current is favored by strong static stability. If the stability is weak between two layers, flows in the upper layer become unstable more rapidly and transfer their energy through fluctuation pressure stresses to the lower layer. In terms of linear baroclinic instability theory, Pedlosky (1979) shows that as the stability, $S = g' \frac{\Delta h}{f_0^2 L^2}$, is decreased, the growth rate is increased for a given scale of waves (assuming that S is below the critical value for the growth of baroclinic waves). By decreasing the upper ocean g' , the tendency is for the flow to become unstable more quickly. It is thus the layer which has the largest g' immediately below it, which tends to exhibit the most coherent mean flow structures, since it receives energy from above but does not as easily transfer it to the next lower layer.

The primary drop in available potential energy in Table 3.1 is from E11 to FCT1, where only the static stability is changed. In FCT1, layer 1 kinetic energy is more rapidly lost to layer 2, reducing the vertical shear, and thus the isopycnal tilt between the layers. Layer 2 energy is less rapidly transferred to layer 3, but these layers are much thicker than layer 1, so that the velocities, and thus the vertical shear, are relatively small anyway. Available potential energy, which is associated with large isopycnal tilt, related through the geostrophic thermal wind to the vertical shear, is thus substantially reduced in FCT1, as well as the other experiments, relative to E11. Chassignet and Boudra (1988) point out that the portion of the kinetic energy associated with the vertical shear flow is directly related to the total available potential energy, and we see a corresponding reduction from the E11 total K.E. in the FCT experiments.

The above conclusions are further confirmed with examination of the individual layer stream function plots, the basin-averaged and horizontal distributions of layer mean and eddy kinetic energy, the layer interface potential energies, and the R.M.S. interface depth deviations. The intermediate layers are consistently more energetic and the bottom layer less energetic in FCT1-4 than layers 2 and 3, respectively, in E11. This is most evident in the most dynamically active regions off South Africa and near the confluence of the northward and southward currents at the western boundary (representing the Malvinas/Falkland and Brazil Currents, respectively). In addition, because the layer 1 retroflection is considerably stronger in E11, the recirculation gyre along the coast and east of Africa is much stronger. Associated with this recirculation is more variability and pumping of energy into

the lower layers than is found in the other experiments. This is especially evident in the bottom layer mean flow patterns, which reveal where the driving of a mean circulation by the eddies is most clearly distinguished. In FCT1-4 the bottom layer mean circulation extends from off the tip of Africa westward to the western boundary. In E11, the anticyclonic portion of this circulation pattern is similarly represented in the South Atlantic but extends a few hundred kilometers northeastward from Africa's tip into the Indian Ocean (Fig. 3.2).

As the model retroflexion is weaker in the new experiments, more of the Agulhas Current water leaks into the South Atlantic than in E11. Much of this additional leakage occurs in Agulhas rings. This is evident in the interface depth fluctuation (R.M.S.) fields (not shown) of the new experiments by a tongue of large interface fluctuation extending from off Africa's tip west northwestward into the subtropical Atlantic. This tongue is evident for all except the lowest interface, whose depth variation is suppressed by the relatively large g' . This tongue is pronounced for FCT1 and FCT2, but has less amplitude in FCT3 and especially in FCT4. The total and fluctuation kinetic energy in the retroflexion region is also reduced from FCT2 to 4, suggesting again that as more upper ocean resolution is added, mechanisms for energy dissipation become more efficient.

One additional factor may account for some of the above-mentioned changes when upper ocean resolution is increased. As the horizontal mean thickness of the top layer is reduced, a larger fraction of it tends to concentrate toward the center of the subtropical gyres. The latitudes at which layers two and three outcrop along the subtropical convergence move northward, and the extent of layer 1 south of Africa becomes less. Layer 1 fluid leaks westward into the Atlantic in rings with relative ease since the retroflexion is not strong, but the fluid attempting to return to the Indian Ocean after circulating through the South Atlantic has little room to do so south of the retroflexion/ring formation area. The net result is that the mean layer 1 thickness becomes weighted toward the subtropical South Atlantic. In the 4-layer experiments FCT2 and FCT3, this weighting is compensated in layer 2. In the 5-layer experiment, FCT4, the compensation is in layers 2 and 3, such that the depths of the intermediate interfaces are not weighted especially toward either the Atlantic or Indian Oceans. The differing mean stratifications to either side of the retroflexion region, on the other hand, which result here from the specification of rather thin isopycnal layers at the top of the ocean in a purely wind-driven configuration, likely play a role in the dynamics of retroflexion and ring formation of these experiments. This may result in the total absence of a mean retroflexion in layer 1 in FCT3 and FCT4. Boudra

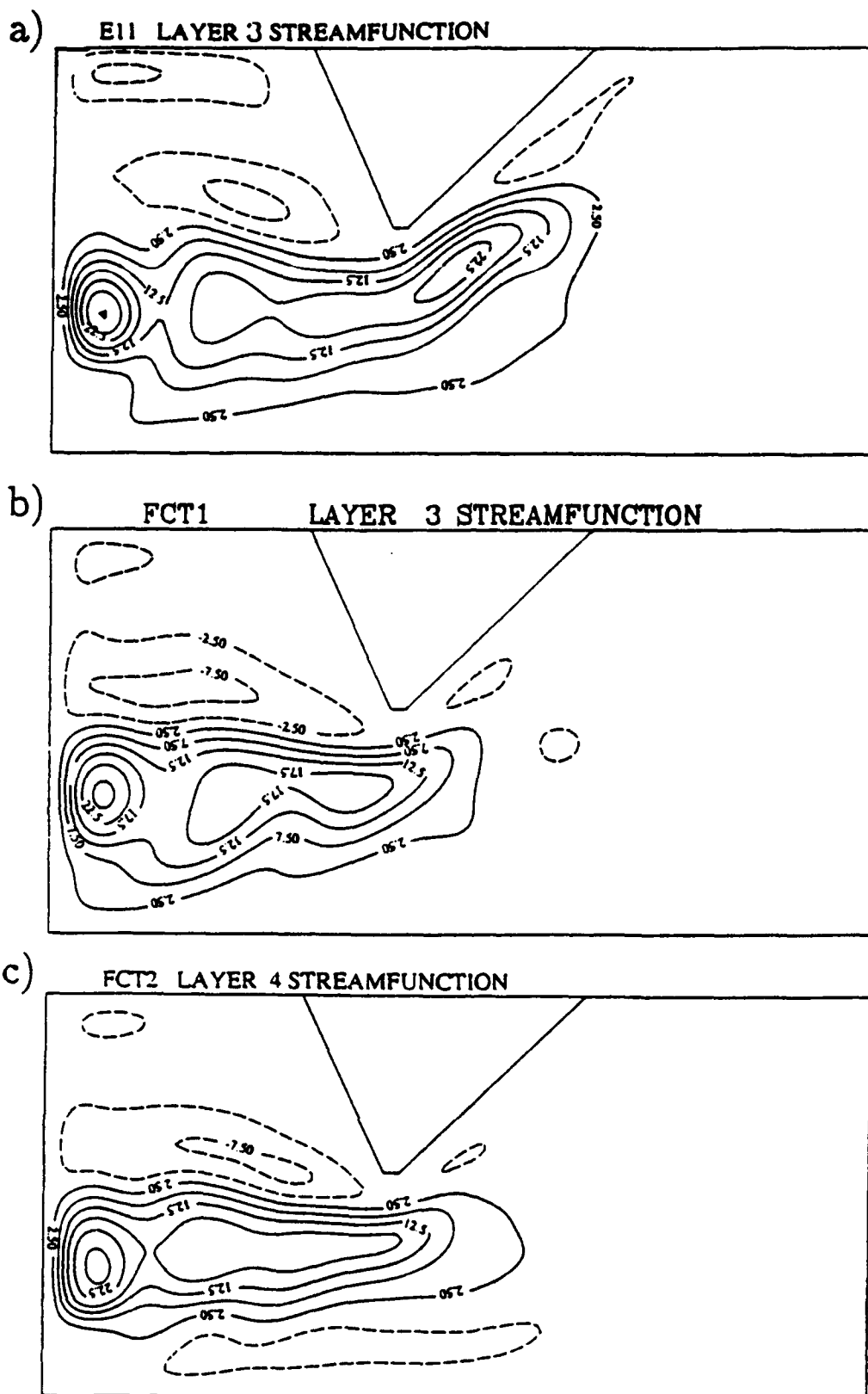
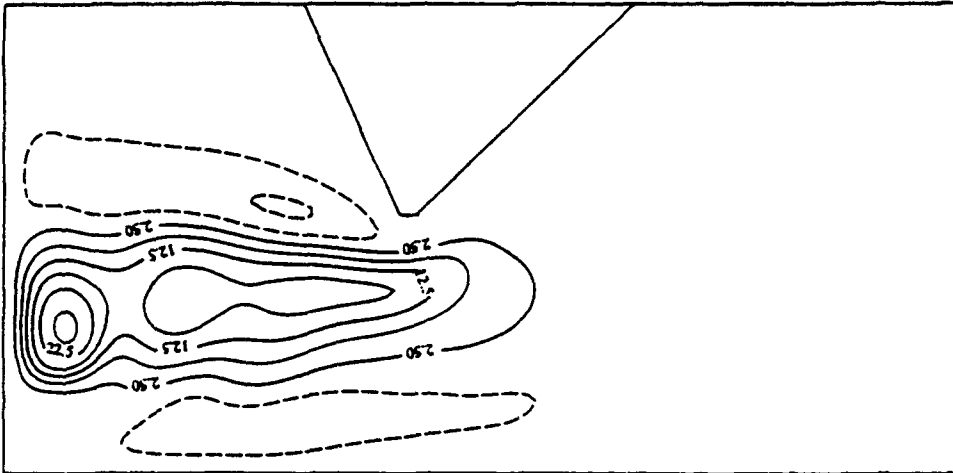


Figure 3.2: Bottom layer streamfunction averaged over four years for experiment E11 a.), FCT1 b.), FCT2 c.), FCT3 d.), and FCT4 e.). The contour interval is 5 Sv.

d)

FCT3 LAYER 4 STREAMFUNCTION



e)

FCT4 LAYER 5 STREAMFUNCTION

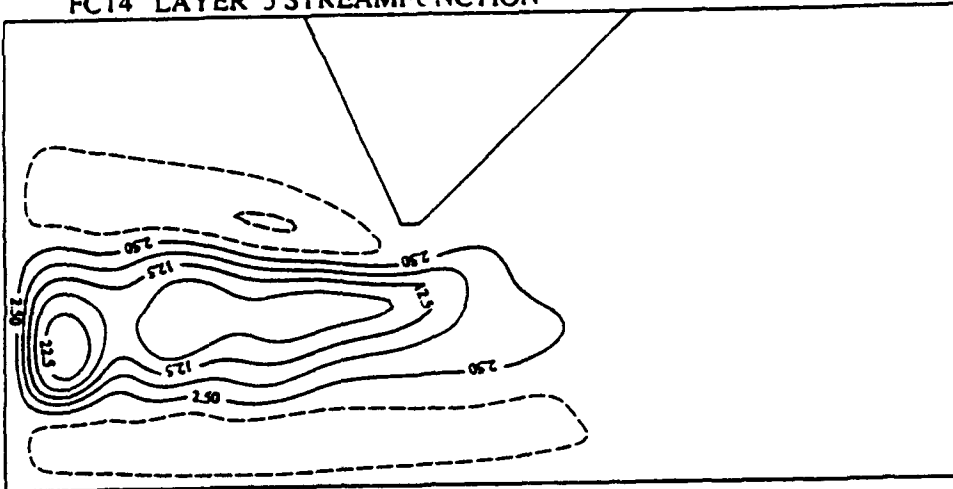


Figure 3.2 cont.

and Chassignet (1988) showed that a strong temporal-mean layer thickness gradient between the southeast Atlantic and the southwest Indian Ocean, such that layer 1 thickness is greatest in the retroflexion region, favors a strong retroflexion. Such a gradient in layer 1 is inhibited from developing in FCT3 and FCT4 for the above-described reasons.

3.3 The Model Agulhas Rings

General characteristics of ring formation, size, and behavior among the experiments are given in Table 3.2. The maximum swirl velocity within the rings and the interface depth change from ring edge to center are good indications of how energetic the rings are. The translation speed is a combination of self-advection due to β and mean flow advection by the South Atlantic subtropical gyre once the rings are free of the African coast. In the remainder of this section, we discuss and illustrate the sensitivity of the model rings to upper ocean resolution and isopycnal outcropping.

Exp.	Diameter (km)	Interface Depth Change (db)	Maximum Swirl Velocity in a newly formed Ring (m s^{-2})	Translation Speed west of Africa (cm s^{-1})	Position of Separation from Agulhas	No. of Rings per 365 day Period
E11	280-300	300-350	1.25-1.5	6.2	Along southeast coast near Africa's tip	3
FCT1	200-240	300	0.75-1.0	7.5	South of Africa's tip.	4
FCT2		200-250	0.75	6.7	S to SW of Africa's tip.	5
FCT3			0.5-0.75		SW of Africa's tip.	
FCT4		150-200		6.5		

Table 3.2: Typical ring characteristics among the experiments. Blanks indicate no change from the previous experiment.

3.3.1 Three Layers (E11 and FCT1)

A typical event of ring formation in the quasi-isopycnal model simulation E11 has been examined in some detail by Chassignet and Boudra (1988) and is one of several rings described and compared with observations in Chassignet *et al.*, (1990). The ring forms along the southeast coast of South Africa/Agulhas Bank near the tip. Its diameter shortly after cutoff from the main Agulhas is ~ 300 km. The maximum swirl velocity is 1.2 m

s^{-1} at a radius of 80 km. The interface 1 depth variation is ~ 300 db from ring edge to center. The ring first propagates westward at 4.3 cm s^{-1} as it rounds the tip of Africa, and then northwestward at 6.2 cm s^{-1} once it is absorbed into the South Atlantic subtropical circulation. Approximately 3 of these rings form per 365 day period in E11, and they account for essentially all of the leakage from the Indian into the South Atlantic Ocean.

In FCT1, the mean retroflecting Agulhas is not as strong and coherent as in E11 (Fig. 3.3). Another important difference is less of a tendency in FCT1 for the current core to separate from the coast upstream from the tip, carrying the isopycnal depth contours off with it. Ou and de Ruijter (1986) have shown that once an inertial current on a β -plane has separated from a coast with the orientation of the east side of the Agulhas Bank (toward the southwest), it has a tendency to make a counterclockwise turn. The mean Agulhas of E11 does this in a fairly abrupt fashion as it passes the tip of the Bank. In contrast, the layer 1 retroflexion of FCT1 occurs over a broad region south of Africa's tip. In some sense, this is a more realistic configuration than in E11, as the real Agulhas Retroflexion is generally located southwest of the tip of the Agulhas Bank, the region where ring formation is most common (Lutjeharms, 1981; Lutjeharms and van Ballegooyen, 1984).

The rate at which top layer fluid leaks westward into the Atlantic is essentially the same in the two experiments. Another important difference, however, is in the layer 2 mean circulation patterns: that is, a small proportion of E11's total Sverdrup interior and retroflexion are found in layer two, whereas they are approximately equally distributed between the top two layers in FCT1. In both cases, essentially all the leakage occurs within rings. In FCT1, both layers 1 and 2 exhibit $\sim 9 \times 10^5 \text{ m}^3 \text{ s}^{-1}$ leakage and in E11 the mean layer 2 leakage is $\sim 4 \times 10^6 \text{ m}^3 \text{ s}^{-1}$. It is apparent then that the transport and energetic expressions of the rings are more distributed over both layers 1 and 2 in FCT1 and are primarily in layer 1 for E11.

Typical instantaneous flow patterns a day or two preceding ring formation in the two experiments are illustrated in Figure 3.4. Rings form and drift into the Atlantic at the rate of ~ 4 per 365 day period in FCT1. Since about the same mean rate of layer 1 leakage is accomplished in E11 and FCT1, the FCT1 rings must, therefore, have less volume and this is apparent in the Figure. The diameters of the two rings in E11 (Fig. 3.4a) are ~ 280 -300 km and in FCT1 (Fig. 3.4b) ~ 200 -220 km. The interface depth gradients around the rings are greater in FCT1, as might be expected due to the much reduced g' , but the total change is ~ 300 m, as in E11. The strongest swirl velocities in the rings cutting off are 0.75 to 1.0 m s^{-1} and 1.25 to 1.5 m s^{-1} in FCT1 and E11, respectively. Similar ratios are seen as the rings propagate into the Atlantic. This is consistent with the above assertion that

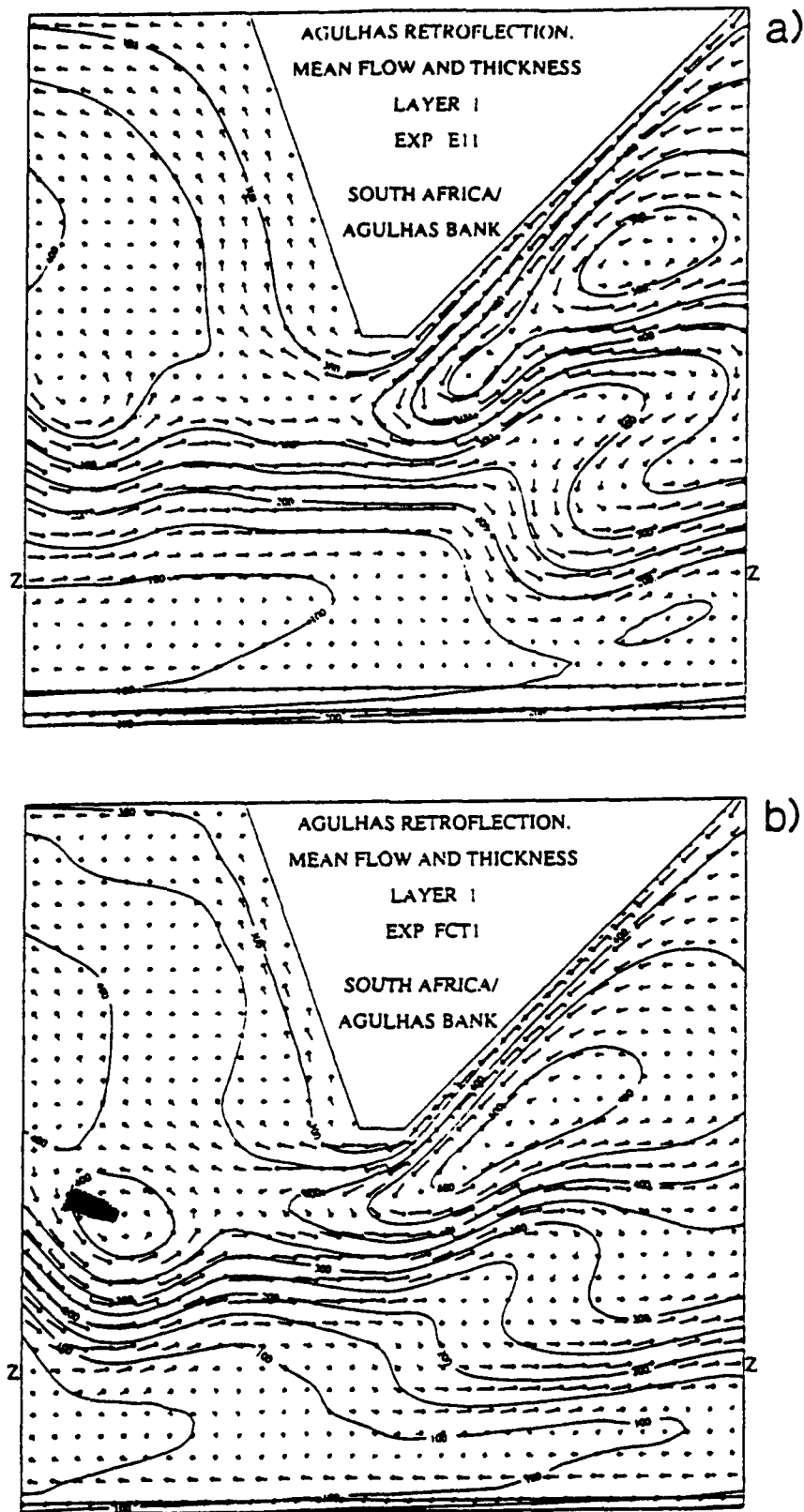


Figure 3.3: The layer 1 velocity and thickness fields averaged over the final 1825 days of the 3650 day experiments E11 a.) and FCT1 b.). Layer thickness is contoured in 50 db intervals. A full length arrow and each additional barb represents 0.25 m s^{-1} flow speed. Flow vectors are indicated for every other grid point. The latitude of wind curl zero is indicated by the Z's at the lower left and right.

the retroflecting Agulhas, from which the rings are formed, is stronger and more coherent in E11. Because the FCT1 rings are smaller and less energetic, they become absorbed into the South Atlantic subtropical gyre and dissipate more quickly. The northwestward translation speed of FCT1 rings in the region west of the Bank is $\sim 7.5 \text{ cm s}^{-1}$, compared with the above-mentioned 6.2 cm s^{-1} for E11 rings, indicating a greater influence of the mean flow on the former.

As the upper ocean stratification is decreased and the intermediate stratification increased within a three-layer configuration, the Agulhas rings become smaller and weaker, but they form more often and in a more realistic position with respect to the tip of the model Agulhas Bank. They also have greater intermediate layer expression, as energy and momentum are transferred more easily from the top into the second layer. The latter is apparently also the reason why the tendency for the interface between the upper layers to outcrop is suppressed, even though the density contrast between them has been greatly reduced. Interface 1 outcropping in FCT1 is sporadic and isolated, tending to occur mainly along the subtropical convergence¹ in the South Atlantic.

3.3.2 Four Layers (FCT2 and FCT3)

In this subsection, we further examine the model ring formation when upper ocean resolution is improved, first by dividing the upper 300 db into two layers of equal mean thickness and then by concentrating the coordinate layers more toward the upper surface. The net g' between the upper layers and the intermediate layer remains $\sim 0.01 \text{ m s}^{-1}$. In these cases, in contrast to FCT1, the first and second isopycnal layer interfaces typically outcrop along the subtropical convergence. In addition, the first interface outcrops around the eastern and northern edges of the subtropical gyres.

A snapshot of the layer 1 and 2 flow and interface 1 and 2 depth fields from FCT2 is depicted in Fig. 3.5. Three Agulhas rings are evident in the Figure. One is forming near the tip and two previously formed rings are propagating northwestward. Both of the interfaces are depressed in these rings, as we expect, but the depth gradient is weaker than for the rings of FCT1 (e.g., see Fig. 3.4b). Further, the total depth change from ring edge to center is 200 to 250 db, also smaller than in FCT1. This is typical of ring characteristics in FCT2-4 and confirms the conclusion of Section 3 that addition of upper ocean vertical resolution allows for more efficient dissipation of the energy input by the wind. In FCT2,

¹The subtropical convergence in the real world divides the subtropical gyres from the northern edge of the Antarctic Circumpolar Current. In the model, we refer to the subtropical convergence as an ever-evolving line dividing the subpolar and subtropical gyres.

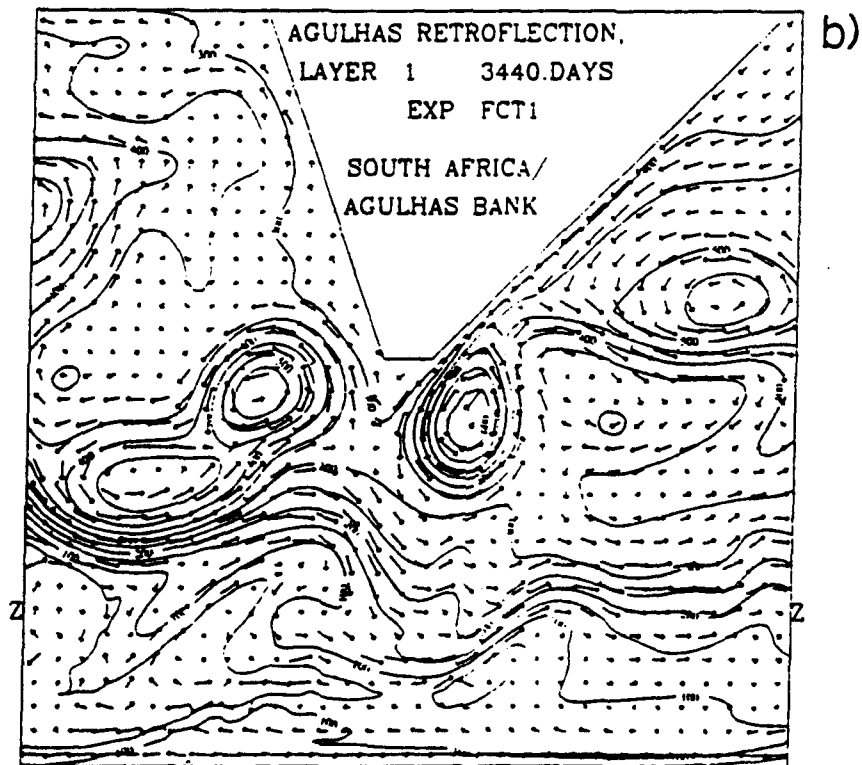
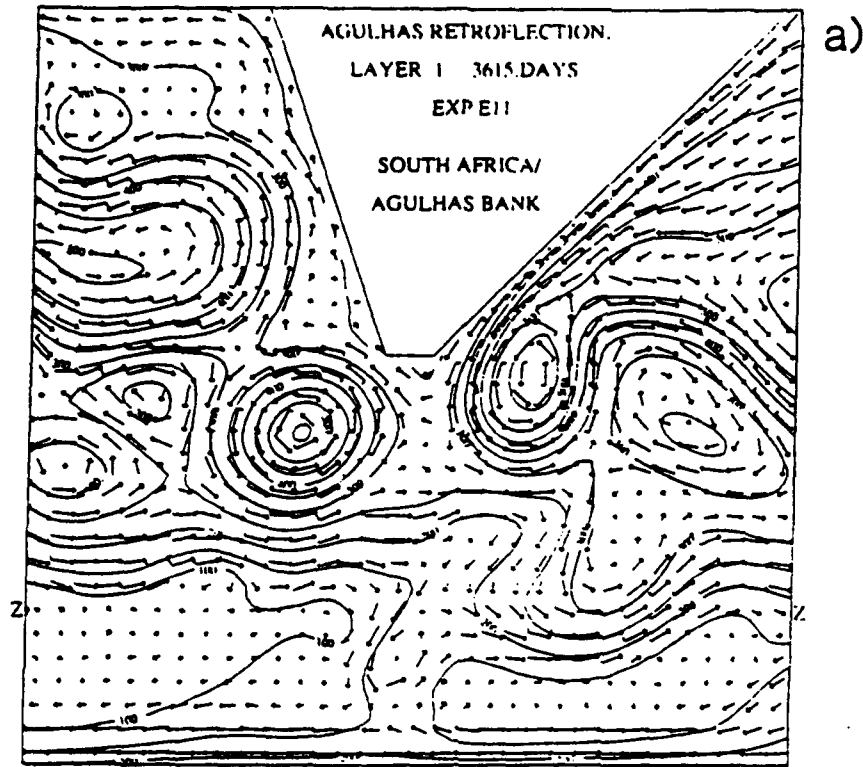


Figure 3.4: Typical layer 1 velocity and thickness fields as a ring is being formed in experiments E11 a.) and FCT1 b.). The contours and barbs are as in Fig. 3.3.

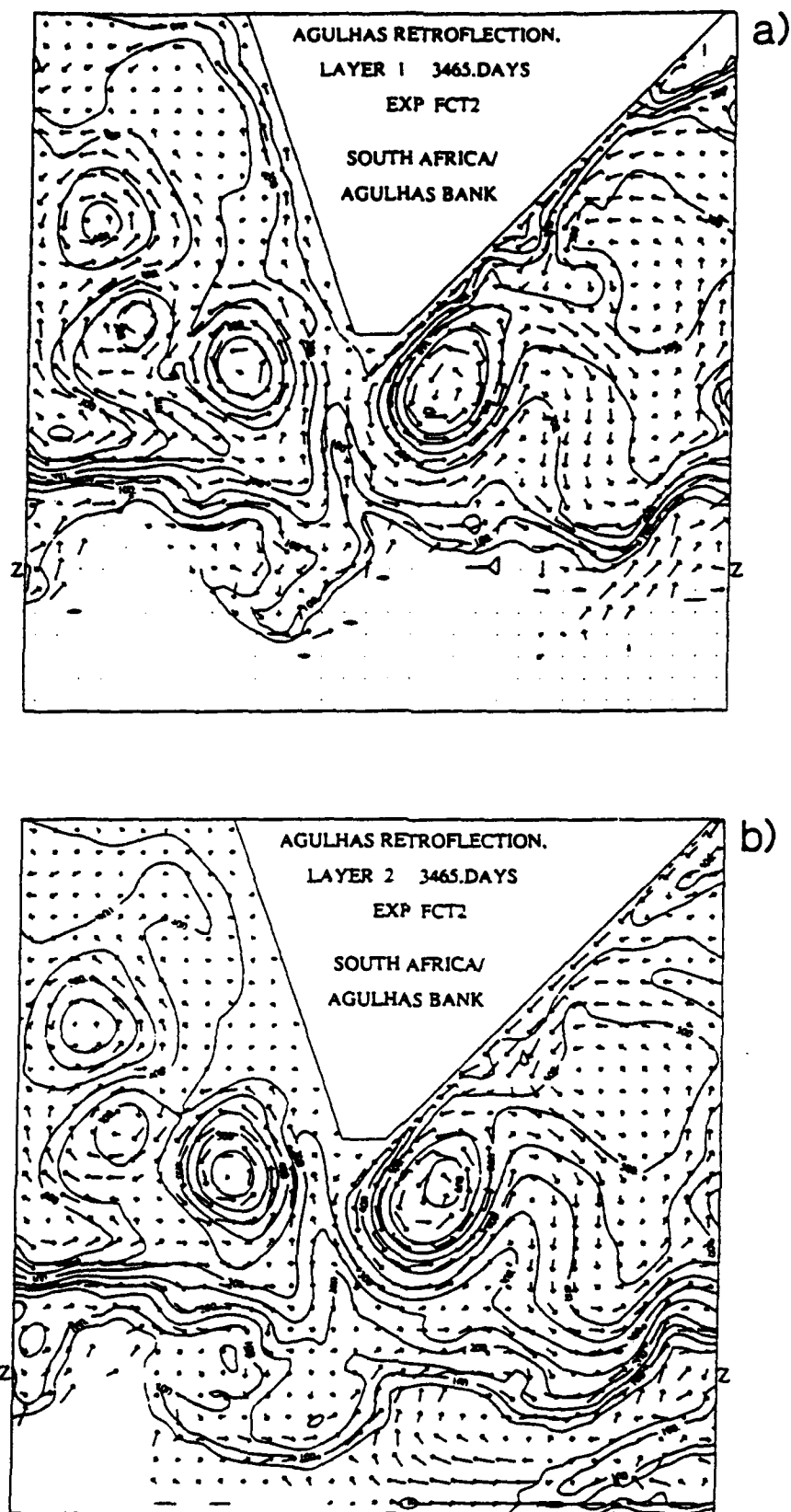


Figure 3.5: Typical layer 1 a.) and layer 2 b.) velocity and interface depth fields for experiment FCT2. The contours and barbs are as in Fig. 3.3. Grid points represented by dots indicate where the layer below is outcropped.

the maximum swirl velocities within newly formed rings are typically 0.75 m s^{-1} . These rings are generally less energetic, than those of FCT1 although they have approximately the same mean diameters, 200-240 km. The mean translation rate is slower than in FCT1: 6.7 compared to 7.5 cm s^{-1} , likely because the mean flow is weaker, but also possibly because the ring's self-advection rate decreases due to its decreased interface displacement (Nof, 1983). The rings typically separate from the Agulhas south of Africa's tip, so that the mean retroflection is broadly distributed there in the east-west direction, especially in layers 1 and 2. The intermediate layer 3 bears the strongest mean retroflection but also $\sim 9 \times 10^6 \text{ m}^3 \text{ s}^{-1}$ of leakage. Thus, as in FCT1, the transport and energetic expressions of the rings in this middle layer are very pronounced. From FCT1 to FCT2, the number of rings forming per 365 days increases from 4 to 5, but the total volume of leakage remains about the same.

Also evident in the Figure is a near-surface tongue of subpolar gyre fluid which is wedged between the developing and the previously formed ring just southwest of Africa's tip. It is quite common for the two water masses to interact in this fashion during ring formation events in experiments FCT2-4 and in the real Agulhas Retroflection region (Lutjeharms, 1988, personal communication).

To encourage additional isopycnal outcropping, the mean thicknesses of the upper two layers are changed from 150 db each to 75 db and 175 db in the four-layer experiment FCT3. The data in Table 3.2 suggests that the impact of this on the structure and behavior of the rings is a slight reduction in maximum swirl velocities to $0.5\text{-}0.75 \text{ m s}^{-1}$. Also, most of the rings are now west of Africa's tip before they cut off from the main Agulhas. From Table 3.1 we note that there is no mean retroflection in layer one, and the vertically integrated mass transport streamfunction (not shown) suggests that the mean retroflection intensity is slightly weaker than in FCT2. The individual layer streamfunctions (Figs. 3.1 and 3.2) suggest that there is no significant change in the rate of leakage from the Indian into the Atlantic. The rings and the mean circulation, then, South of Africa's tip are less energetic as resolution is concentrated toward the upper surface, suggesting again that the energy input by the wind is dissipated more effectively.

An illustration exhibiting the FCT3 preference for a more westerly ring formation position is given in Figure 3.6, where instantaneous mass and flow fields for layers 1 and 2 are depicted just prior to ring cutoff. Note that a portion of the Agulhas turns back toward the Indian Ocean near the southeast tip of the shelf break geometry, but another significant portion continues around the outer edge of the developing ring circulation. Between the two is an intrusion of subpolar gyre fluid as much as 240 km north of the wind curl zero

latitude. This intrusion, strongly evidenced in the 2nd interface depth (Fig. 3.6b) contours, is associated with and is likely playing an important role in the ring formation event. The subtropical front is sharply inclined in general, but especially here where the depth of the 2nd interface increases from less than 50 db to 400 db over a distance of ~ 60 km.

3.3.3 Five Layers (FCT4)

The rings of FCT4, in which two upper layers now have mean thicknesses of 75 db, the third 100 db, the intermediate layer 950 db, and the bottom layer 3800 db (as in all experiments), are even less energetic than in FCT3. Horizontal plots of total and eddy kinetic energy (not shown) reveal that the retroflection region is 20-30% less energetic than in FCT3. From column 3 of Table 3.2 we note that the interface depth change from the ring edge to center is typically only 150 to 200 m, and this is true for all three of the upper ocean interfaces. The maximum swirl velocities are generally little more than 0.5 m s^{-1} . Again, this further increase in upper ocean resolution has enhanced the transfer of energy input by the wind to the intermediate layer, as well as allowed for more efficient dissipation through release of instabilities. Also, as pointed out at the end of Section 3, the energetic and dynamical character of the retroflection region may be significantly influenced in FCT3-4 by the fact that layer 1 fluid tends to accumulate in the South Atlantic subtropical gyre, finding it somewhat difficult to return to the Indian Ocean in the short distance south of Africa to its outcrop. This configuration is an artifact of the lack of thermohaline forcing in the model. In actuality, some of the warm fluid leaking from the Indian into the Atlantic returns to the Indian Ocean as modified denser water after circulating through the South Atlantic. An accounting for such conversion must be made to determine the effect of the non-thermohaline forced circumstances on the retroflection dynamics. We will return to this issue in the closing remarks.

Of particular significance in the experiments with more upper ocean resolution is the realistic tendency for rings to cut away from the Agulhas farther south and west than in E11 and FCT1. This is perhaps the factor most responsible for increased interaction with the fluid from the subtropical/polar front in FCT2-4. Such volatile interaction in FCT4 is illustrated in Figure 3.7, where layer 3 flow and interface 3 depth are depicted at two instants 25 days apart. As in Figure 3.6, a pronounced intrusion of subpolar fluid is involved in the ring formation event near Day 3440 (Fig. 3.7a). In the subsequent snapshot (Fig. 3.7b), this intrusion has shifted eastward where it is influencing the formation of the next ring. This interaction in the model is especially significant because satellite imagery commonly displays filaments of cold surface water from the northern edge of

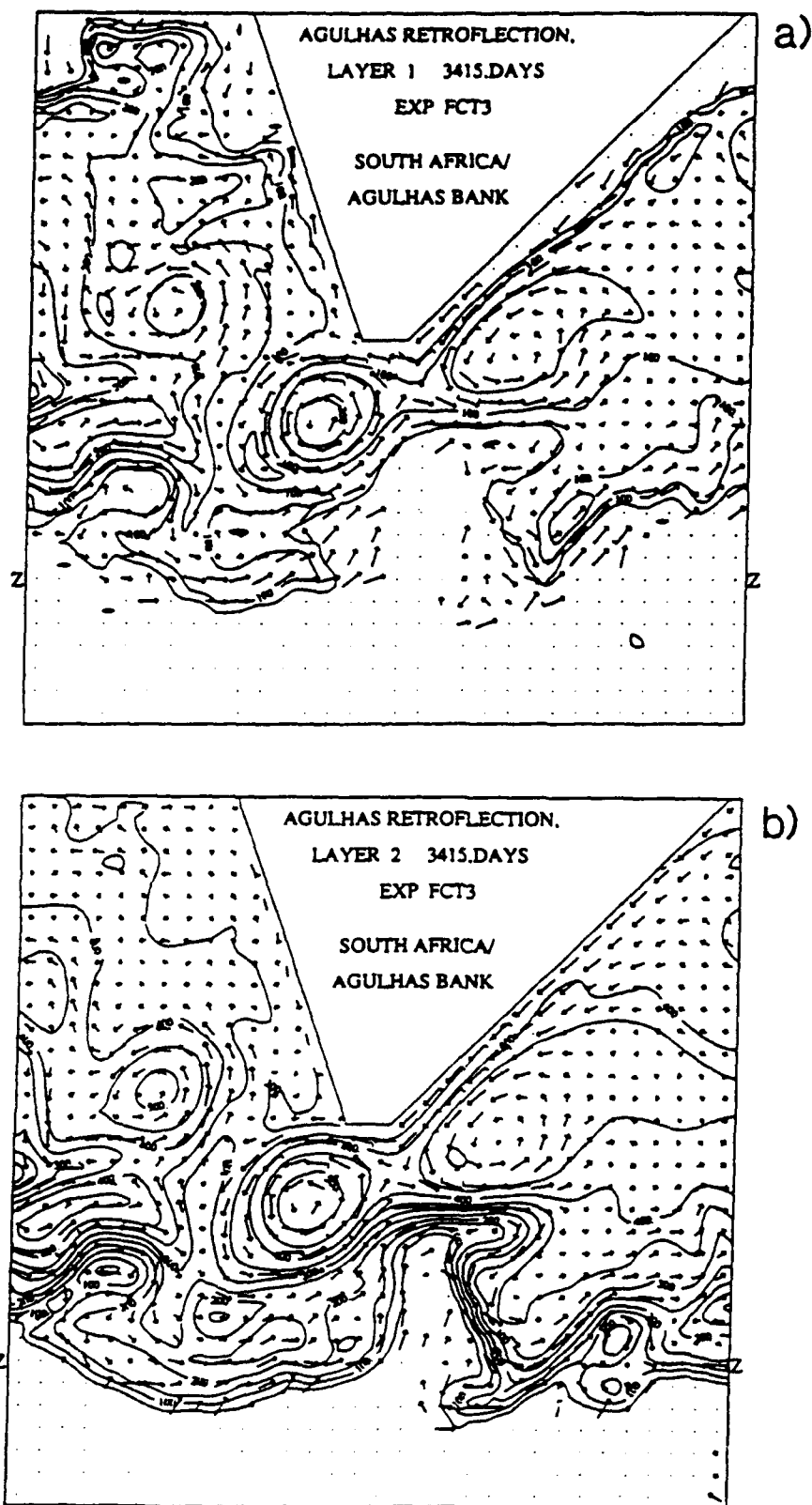


Figure 3.6: Instantaneous layer 1 a.) and layer 2 b.) velocity and interface depth fields for experiment FCT3 very close to an event of ring cutoff. The contours and barbs are as in Fig. 3.3 and the grid points represented by dots indicate where the layer below has outcropped.

the ACC between the Retroflection and a newly formed ring (Lutjeharms, 1988, personal communication).

3.4 Summary

The sensitivity of Agulhas retroflection and ring formation in an idealized model of the South Atlantic-Indian Ocean to increases in upper ocean vertical resolution and isopycnal outcropping has been explored. Here we have described a first series of experiments with a pure-isopycnic coordinate model which handles the outcropping of coordinate surfaces in a robust fashion, replacing the quasi-isopycnic coordinate model used in previously reported work. To encourage isopycnal outcropping, first, the relative strengths of the interface density jumps in the 3-layer framework are reversed. The uppermost interface g' is reduced from 0.02 to 0.01 m s^{-2} , but a major impact is the more rapid transfer of energy from layer 1 to 2, as well as more efficient dissipation of energy input by the wind. Thus, isopycnal outcropping is not a predominant feature of the experiment. The retroflection is slightly weakened and the rings formed are smaller and less energetic than in the case with the stronger upper interface g' , but they have more intermediate layer expression.

When the number of layers is increased first to 4 and then 5, the strength of the retroflection and the energetic magnitudes of the retroflection activity continues to decrease. The rings tend to separate from the main Agulhas more often and at a more southwesterly position, however, which is a trend more toward the position where real Agulhas rings form with respect to the Agulhas Bank. Likely because of this more southerly location, intrusions of subpolar origin fluid are quite often found playing an active role in the ring formation events, as is known to happen in the Retroflection area.

A preliminary conclusion from these results is that reduced static stability and improved vertical resolution near the model ocean surface both lead to more efficient dissipation of the energy input by the wind at the surface. In the first case, the upper ocean flows become unstable more rapidly, and in the second, the release of instability is apparently better resolved. A thorough energetics analysis of the experiments would be required to verify the second assertion. Chassignet and Boudra (1988) found coherent peaks in basin-averaged barotropic and baroclinic energy conversion to coincide with events of Agulhas ring cutoff in the quasi-isopycnic experiment E11, and they concluded that a weak mixed barotropic/baroclinic instability is associated with ring formation in the experiment. Due to the relative weakness of the rings generated in the experiments FCT2 to FCT4 here, it seems that peaks in the basin-averaged energetics would be less prominent and that

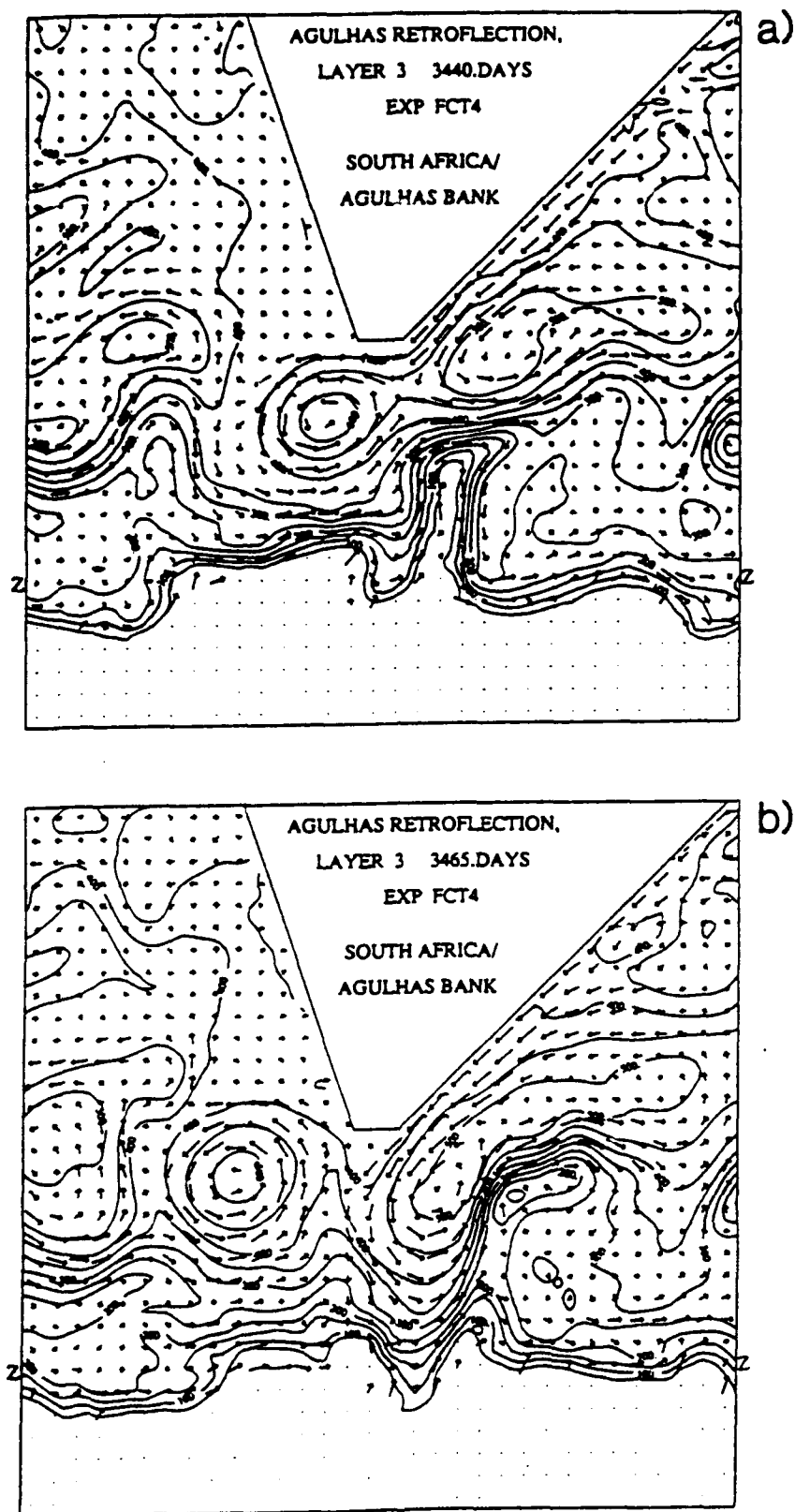


Figure 3.7: Instantaneous layer 3 flow patterns and interface 3 depth fields 25 days apart in FCT4. Note the intrusion of subpolar fluid associated with development of two rings. The contours and barbs are as in Fig. 3.3 and the grid points represented by dots indicate where the layer below has outcropped.

dynamical instabilities play a less energetic role in the formation process. What is mainly apparent here is that the onset of instabilities occurs at a lower level of basin available potential energy, preventing the circulation from reaching the energetic intensity of E11.

Chapter 4

Large Basin Experiments

4.1 Introduction

In this Chapter we continue to increase the realism of the Agulhas retroflection model by (1) extending the basin size to more realistically reflect the scales of both the Southern Indian and the South Atlantic basins, and (2) more realistically modeling the African coastal boundary by using the 1000 m isobath to represent the Agulhas shelf break. Our goal is to compare the model results with recently gathered ocean measurements of the Agulhas region to investigate how well the model represents the real ocean.

Chassignet (1988) suggested that the unrealistically small basin size and coastal geometry of previous experiments did not facilitate such comparisons in the past. With the new configuration, the wind stress curl zero is located approximately 1000 km to the south of the African continent. This corresponds to the annual mean position of the curl zero from the Hellerman and Rosenstein (1983) data. This situation moves the subtropical convergence to a more southerly position which leaves more room to the south of the continent for the current to perform a retroflection. Additionally, the expanded size of the Atlantic basin is such that rings rounding the tip of Africa can travel freely in a better represented South Atlantic circulation. Two experiments will be described. Comparisons between the observed mean and eddy flow derived from current meter moorings and model mean and eddy flows over the final four years of each ten year experiment will be discussed. Spectral characteristics of the mooring data and model data will also be compared. In addition, trajectories of model Agulhas rings will be compared to observed drift paths of real Agulhas rings as measured from satellite sea surface height measurements. We also wish to investigate the effect of isopycnal interface outcropping on the model solution through comparisons between models. Chassignet and Boudra (1988) described the energetics of rings

in experiment E11 and in Chapter 3 above we described some preliminary experiments to investigate outcropping and increased vertical resolution. Both Veronis (1973) and Ou and de Ruijter (1986) included thermocline outcropping in their models of the Agulhas Current. In each of these models, the Agulhas separated from the coast when the lower layer outcropped at the sea surface. The enhancement of vertical resolution in the new large basin experiments, along with the inclusion of the FCT algorithm in integrating the continuity equation allows us, for the first time, to incorporate such thermocline surfacing in a primitive equation (PE) numerical model of the Agulhas. First we will discuss various recent observations gathered in the Agulhas current area to set the stage for our model comparisons with observations. Next the results from the models will be described and finally, a discussion about the results, including comparisons to observations as well as to the experiments previously described in Chapter 3, will be offered.

4.1.1 Agulhas Current Observations

In this section we discuss recent observations gathered in the Agulhas region. We will compare, both quantitatively and qualitatively, these observations with our model results. Figure 4.1 shows the mean velocity vectors from a two year period during which current meters were moored in the Agulhas region (J. Luyten, personal communication). Strong southwestward flow (70 cm sec^{-1}) is apparent along the Agulhas shelf break in the Agulhas current core. Weaker southwestward and westward flow dominates north of 39° S , while south of 40° the flow appears, in the mean, to be directed towards the east. Superimposed on the mean flow figure is one realization of the presumed path of the Agulhas, obtained in February/March 1985 by navigating along the intersection of the 15° isotherm and the 200 m depth surface (Bennett, 1988). The path was navigated at the time when the moorings were put in place. The coincidence of the two year mean vectors with the observed path is remarkable and suggests that the path was fairly consistent throughout the averaging period.

Eddy kinetic energy has been calculated from the two year current meter time series (Fig. 4.2). Although these data are sparse, they illustrate some interesting features about the eddy activity in the Agulhas region. In the upper ocean, a maximum in EKE of over $2800\text{ cm}^2\text{ sec}^{-2}$ is found just south of the shelf break at mooring 839. High EKE is found to the west of this maximum at mooring 838, and values of EKE drop off in all directions with a minimum along the shelf break in what we can consider the mean current core. The Agulhas region has been termed one of the most variable regions in the world oceans, mostly on the basis of satellite sea surface height variability measurements and indeed,

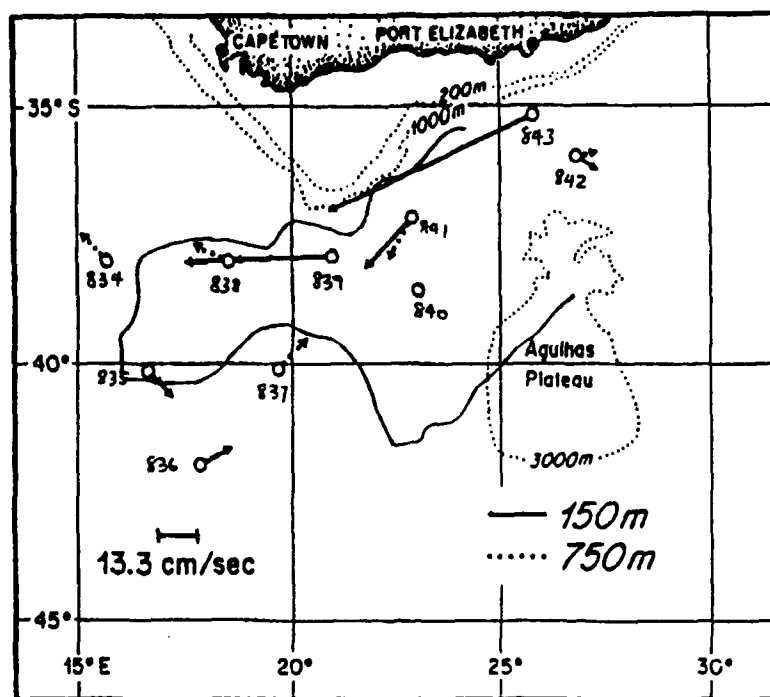
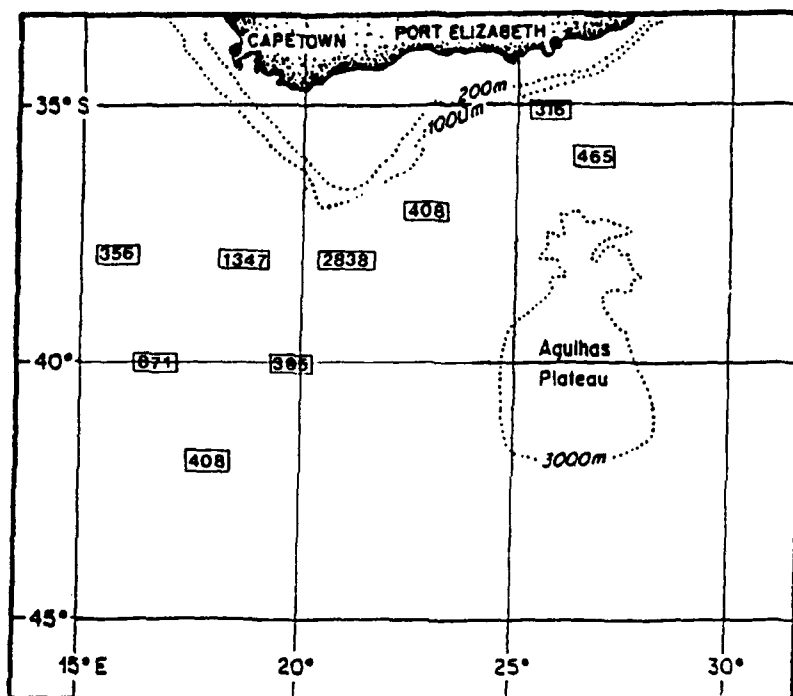


Figure 4.1: Mean current vectors computed from a two year velocity time series. Overlaid is a path of the Agulhas Current derived by navigating along the intersection of the 15° isotherm and the 200 m depth contour.

the present data confirm a region of highly variable flow. The high EKE values compare with estimates of those in the Gulf Stream determined from surface drifters. In the most energetic regions of the Stream, EKE values of over $2000 \text{ cm}^2 \text{ sec}^{-2}$ are seen (Richardson, 1983). In the deep ocean, (below 4000 m) EKE measurements (Fig. 4.2 b.) of over $110 \text{ cm}^2 \text{ sec}^{-2}$ are observed in the region of highly energetic surface eddy activity. Here again, the EKE values drop off away from this maximum region along 37° S. Again comparing with the Gulf Stream, abyssal eddy kinetic energy measurements of the North Atlantic exhibit values of around $120 \text{ cm}^2 \text{ sec}^{-2}$ beneath the Gulf Stream Extension (Schmitz, 1984). The present data suggest a region of high eddy energy just south of the African continent, and are consistent with the shedding of eddies by the Agulhas current.

Kinetic energy spectra have been computed for the two moorings along 37° S which display the greatest variability in the data. Figure 4.3 shows the variance conserving spectra of a.) mooring 838, longitude 18.1° E, and b.) 839, longitude 21° E, at a nominal depth of 200 m. In this figure we can see that mooring 839 is somewhat more energetic than 838 but both moorings exhibit peaks at a period of 37 days. The two time series, however, show little squared coherence (Fig. 4.3 c) at this depth suggesting scales less than 265 km. Figure 4.4 shows the spectra of kinetic energy at two depths on mooring 838. On the left is the energy spectrum at 200 m and on the right that at 4000 m. The decrease

a) Eddy Kinetic Energy of the Upper Ocean
($\text{cm}^2 \text{sec}^{-2}$)



b) Eddy Kinetic Energy of the Deep Ocean
($\text{cm}^2 \text{sec}^{-2}$)

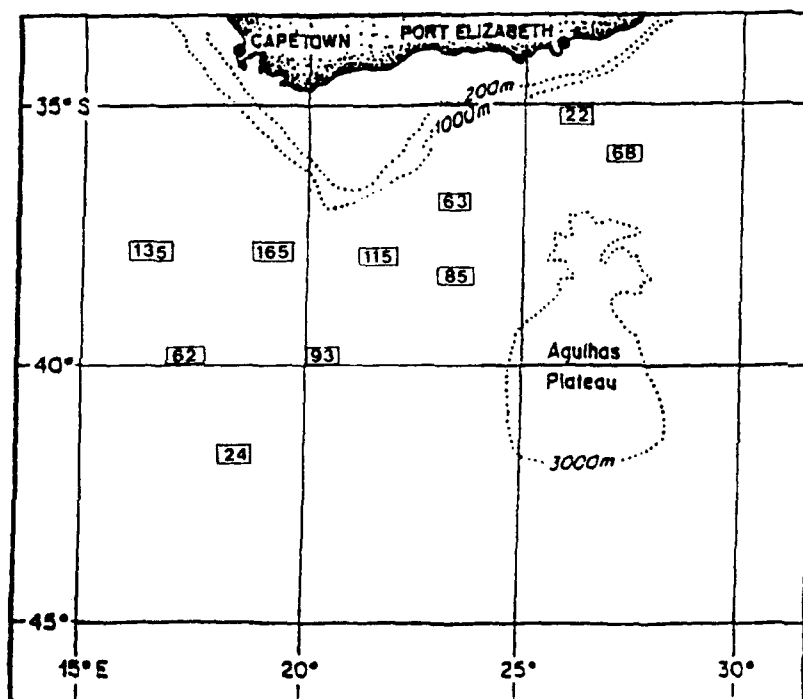


Figure 4.2: Values of mean eddy kinetic energy at the current meter moorings in a.) the upper ocean (200 m) and b.) the deep ocean (5000 m).

in energy is evident at depth along with a slight shift in the energy peak, occurring at 32 days at 4000 m. The squared coherence between these depths is low for all periods under 100 days. Above 100 days, the two series are only marginally coherent. Figure 4.5 shows the spectra at two depths for mooring 839. Again on the left is the spectrum at 200 m and on the right at 4000 m. A decrease in energy is again evident at depth along with a shift in the energy peak, occurring at 20 days at 4000 m. Also, in the deep ocean, mooring 839 exhibits high energy at periods greater than 50 days. Figure 4.5 c.) shows that mooring 839 is vertically coherent between periods of 4-10 days but not so above 10 days. Gordon and Haxby (1989), using satellite altimeter data, and Chassignet (1988), from satellite sea surface temperature (SST) data, have estimated that approximately five eddies per year are shed by the Agulhas Current. Lutjeharms and van Ballegooyen (1987) arrived at a slightly higher estimate of six to nine eddies per year, also on the basis of SST data. If we assume that variability seen in moorings 838 and 839 is due to the passage of Agulhas eddies past the moorings, we can estimate the number of eddies shed in a year based on the current meter data. Since the anticyclonic phase and the cyclonic phase of the eddies contributes equally to the kinetic energy spectra and since the peak energy occurs at approximately 37 days, eddies would pass the current meter with a period of 75 days. This would imply an eddy shedding frequency of five per year. Later in this Chapter we will compare these results with those obtained from our models.

As mentioned above, measurements of satellite sea surface height variability suggest that the Agulhas region is one of the most variable in the world oceans. Figure 4.6 (Gordon and Haxby, 1989) shows the root mean square (RMS) variability of the geostrophic velocity during the period November 1986 to November 1987. These data show that the region of maximum variability exhibited in the Agulhas region occurs between $37^{\circ} - 39^{\circ}$ S and $19^{\circ} - 20^{\circ}$ E. This agrees well with the moored current meter derived EKE measurements shown above.

The fate of Agulhas eddies after they round the tip of Africa has been traditionally difficult to discern since the sea surface temperature signal is erased very quickly due to the high heat flux in the eastern South Atlantic. Consequently, satellite SST images are of limited use after the rings have propagated into the Atlantic. Recently, however, satellite measurements of sea surface height from altimetry has been used to detect Agulhas rings in the South Atlantic (Gordon and Haxby, 1989). Figure 4.7 depicts the tracks of various Agulhas eddies after they were shed from the formation region south of Africa as seen in data taken from Geosat altimeter measurements. After exiting the Agulhas region, the eddies appear to drift into the subtropical South Atlantic on a westward or northwestward

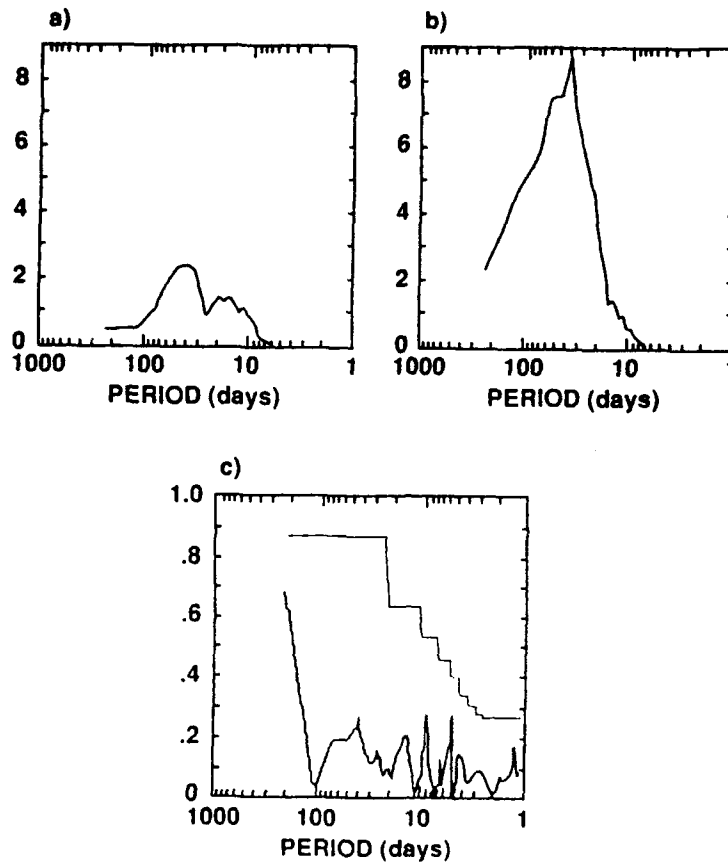


Figure 4.3: Kinetic energy spectra in the upper ocean from moorings a.) 838 and b.) 839 (units are in $10^5 \text{cm}^4 \text{sec}^{-4}$) and c.) squared coherence (confidence interval is 95 %).

course. The figure shows that some eddies can be detected almost all the way across the Atlantic basin.

4.1.2 Experimental Design

Table 4.1 shows the parameters of the two experiments used in this study. Experiment MERC1 is essentially the same as experiment E11 and experiment FCTMERC is the same as experiment FCT4 above, the differences being the inclusion of the large domain and realistic coastline. The eddy viscosity coefficient for FCTMERC was increased to $500 \text{m}^2 \text{sec}^{-1}$ to prevent nonlinear numerical instability which was a problem with smaller viscosity values. Comparisons of both experiments MERC1 and FCTMERC with observations will be carried out to investigate the relationship between the models and the real ocean.

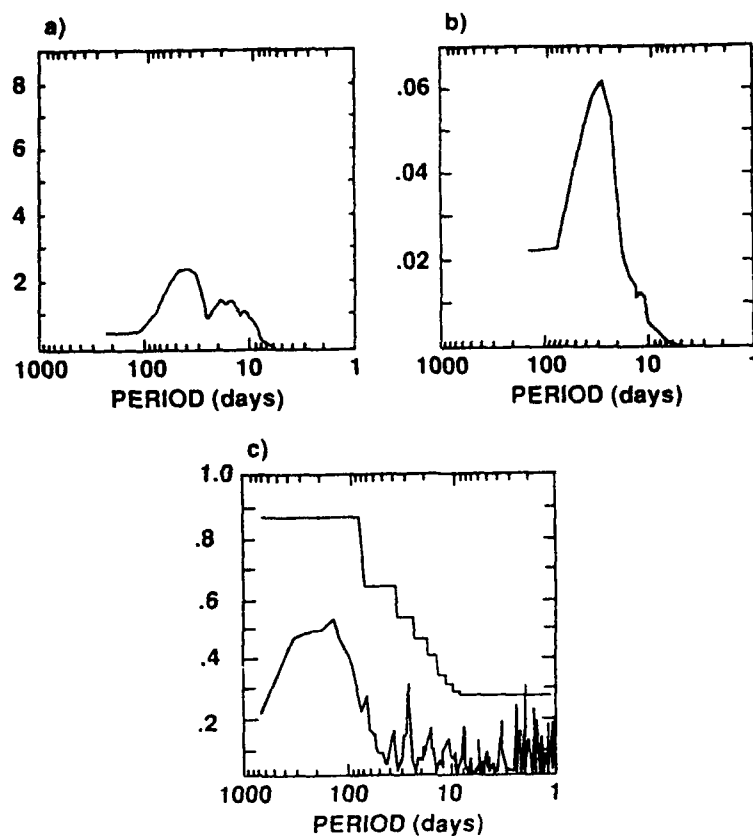


Figure 4.4: Kinetic energy spectra from mooring 838 a.) upper ocean, b.) deep ocean (units are in $10^5 \text{cm}^4 \text{sec}^{-4}$) and c.) squared coherence (confidence interval is 95 %).

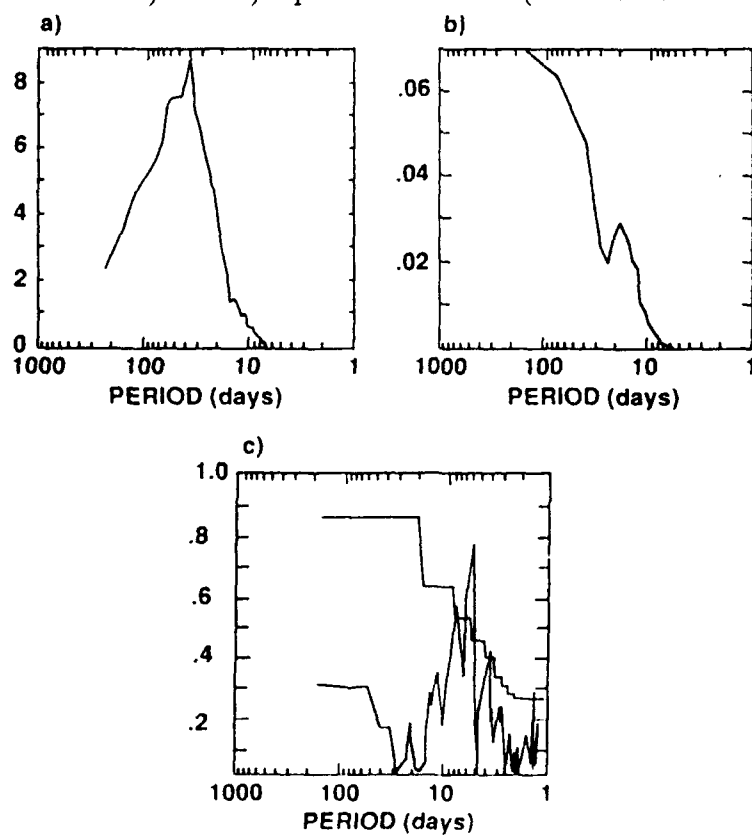


Figure 4.5: As in Fig. 4.4 for mooring 839.

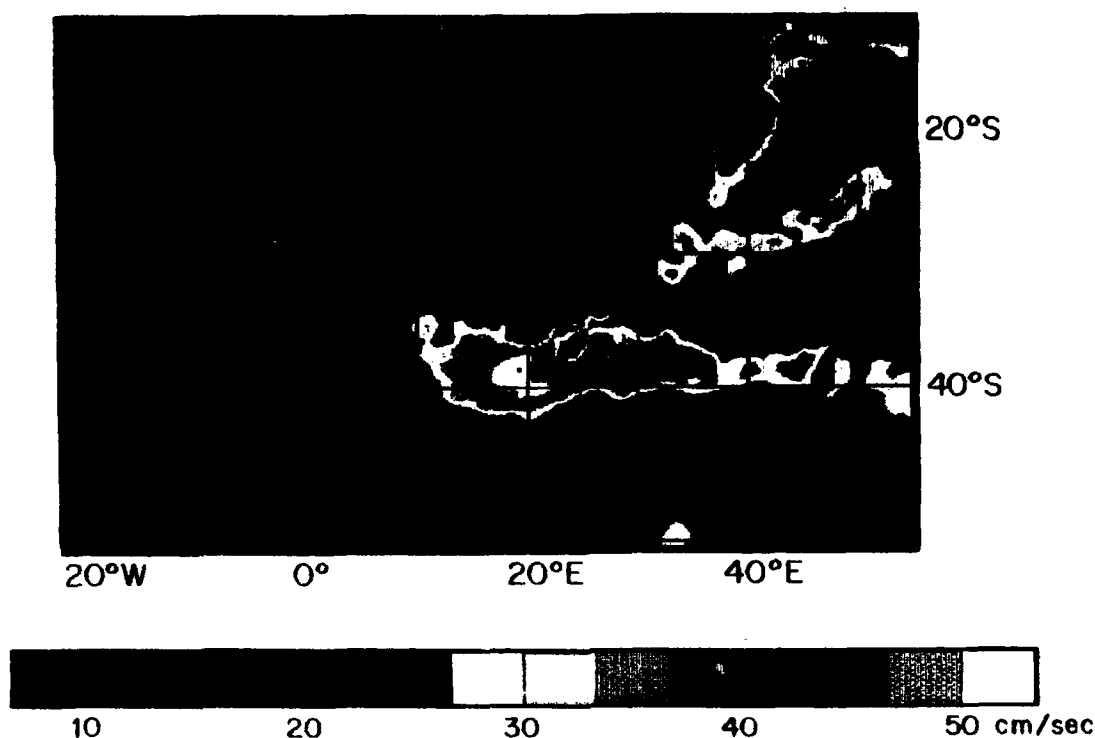


Figure 4.6: RMS variability of the geostrophic velocity for the South Atlantic/Agulhas region during the period November 1986 to November 1987 as measured by the Geosat altimeter (from Gordon and Haxby, 1989). The dots are the locations of moorings 838 and 839. Crosses indicate maxima in variability from the models described in this Chapter.

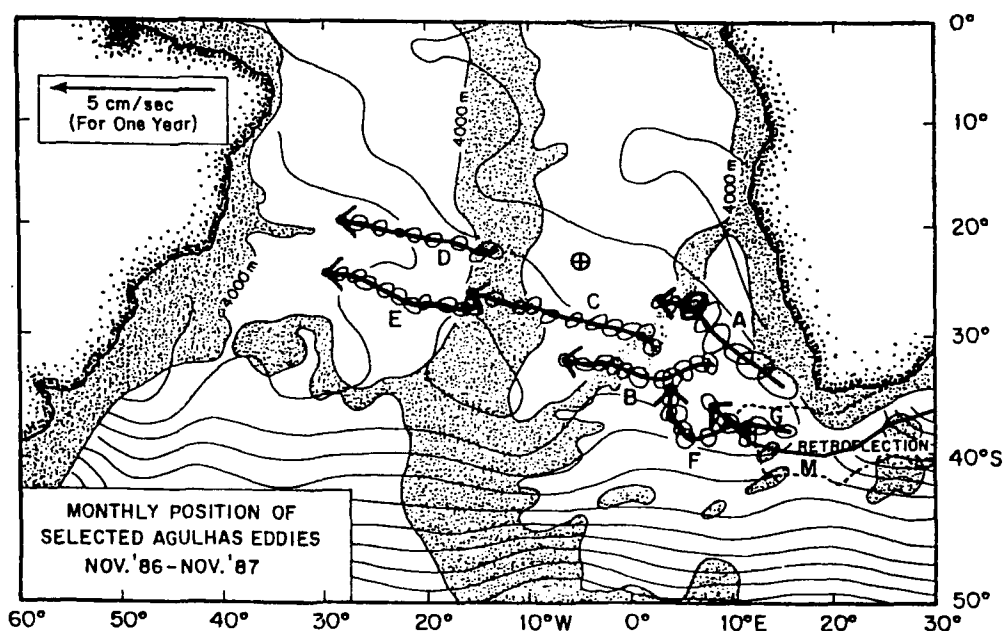


Figure 4.7: Trajectories of seven selected eddies, labelled A through G as measured by the Geosat altimeter (from Gordon and Haxby, 1989). The track labeled M is a typical eddy track from the models described in this Chapter.

Exp.	Mean Layer Thickness (db)	Interface g' ($msec^{-2}$)	A_m (m^2sec^{-2})	Bottom Drag	African B.C.
MERC1	300	0.02	300	10^{-7}	NS
	900	0.005			
	3800				
FCTMERC	75	0.003	500		
	75	0.003			
	100	0.003			
	950	0.016			
	3800				

Table 4.1: Parameters of the two experiments described in Chapter 4. Blanks indicate no change from previous experiment.

4.2 Results

4.2.1 Experiment MERC1

Figure 4.8 depicts the mean flow over the last four years of the ten year experiment MERC1. General agreement with the current meter mean flow vectors is found in the Agulhas core with strong southwestward flow. Directly south of the shelf break, however, the model produces very weak flow towards the east in the mean, in contrast to the westward mean flow found in the current meter data. We will discuss the reason for this discrepancy later in this Chapter. South of 40° S, the model mean flow agrees well with the mean flow derived from the observations.

Maps of EKE in the a.) upper layer and b.) lower layer of the three layer model are shown in Figure 4.9. The upper layer map exhibits areas of EKE that are of the same order of magnitude as observed in the Agulhas region but the model seems to exhibit most of its variability far up the shelf break instead of to the south of it as seen in the observations. Deep EKE exhibits a similar feature of approximately correct magnitude but the maximum is seen well up the African coast, directly beneath the maximum in the upper layer.

To see the reason for the difference in location of high eddy activity between the model and the observations we look at a series of instantaneous flow field pictures from year 9 of the model run (Fig. 4.10). As in previous versions of this model, the Agulhas flows down the shelf break, separates from the coast, retroflects, and periodically cuts itself off to form an Agulhas ring. As we see in the series of "snapshots" of the flow field, the current core separates well upstream of the tip of Africa and rings are formed along the coast. These rings subsequently flow along the coast and around the tip of Africa into the Atlantic Ocean. The region of high EKE seen in Figure 4.9 agrees well with this region of ring formation.

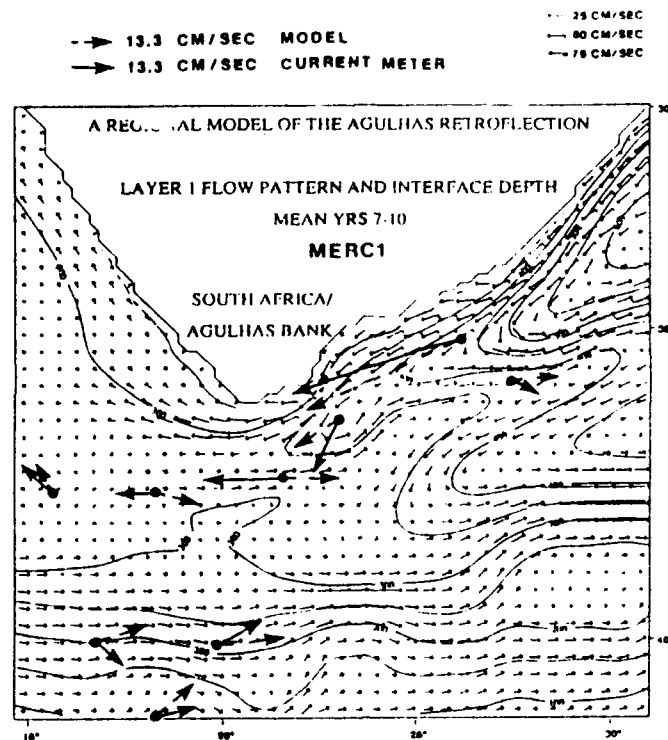


Figure 4.8: Mean flow vectors from current meter data and experiment MERC1. Heavy solid arrows depict current meter data. Heavy dashed arrows depict model data at the current meter location. Small arrows are model velocities. Contour lines indicate model mean interface depth in meters.

The reason for this premature retroflection of the current is not entirely clear. Boudra and Chassignet (1988) concluded that it is the change in the vorticity balance of the current which causes the Agulhas to retroflect with the frictional African coast acting as a vorticity sink to balance the β -induced gain in relative vorticity along the shelf break. When the current flows past the tip of Africa, it loses this sink and any additional gain in planetary vorticity caused the Agulhas to turn back into the Indian Ocean. In the present case, the Agulhas core never reaches the tip of the continent. Instead, the current begins to separate well up the coast, north of 35° S. As soon as the current separates, the above described vorticity balance change occurs and the current turns back into the Indian basin. Two possibilities exist to explain this discrepancy. First, the model may not be inertial enough to allow the separated Agulhas to reach the tip of Africa. Secondly, many theories of western boundary current separation maintain (Parsons, 1962; Veronis, 1973) that an integral part of any separation is the surfacing of the thermocline along the boundary. This is prevented from happening in this particular model. Both possibilities will be explored by changes made in the five layer model to be described below. The thinning of the upper layers of that model reduces the Rossby number, thereby providing a more inertial setting for the current. Additionally, the application of the FCT algorithm allows

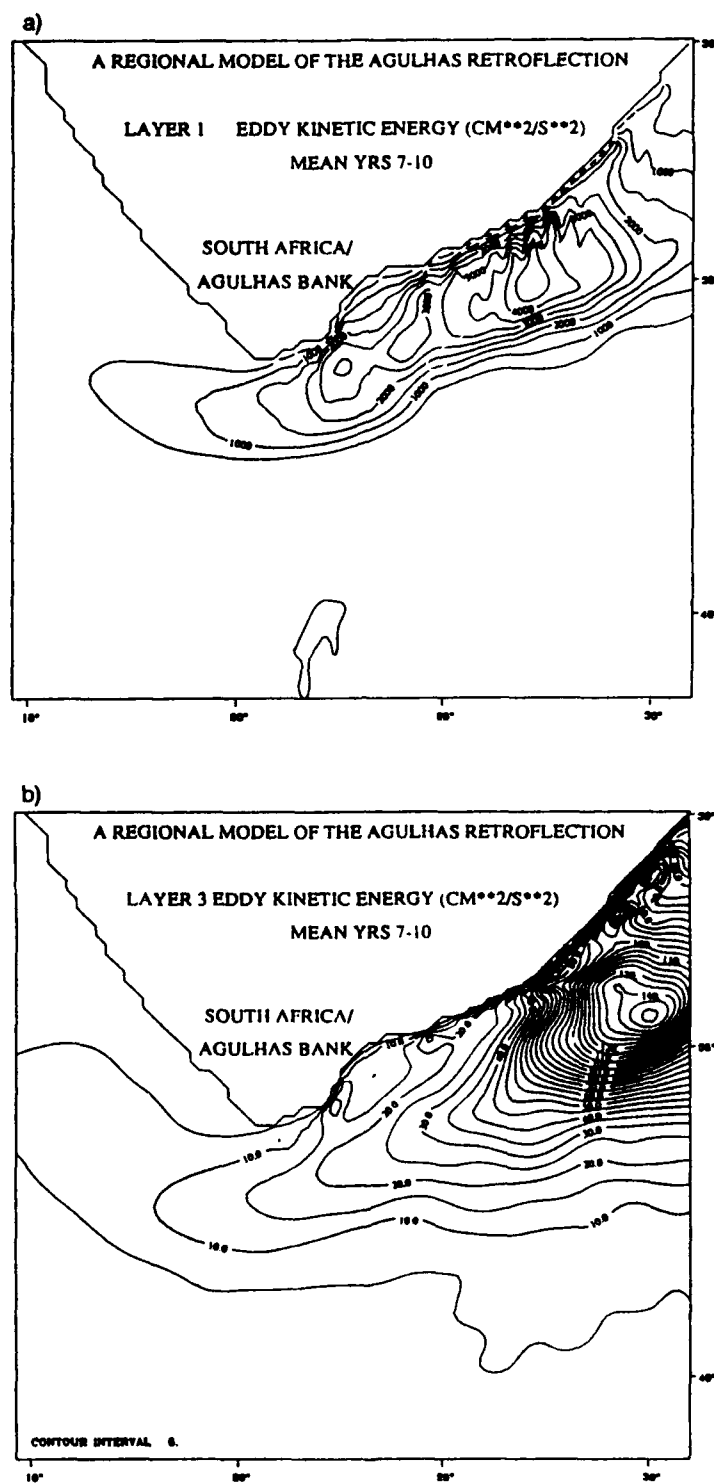


Figure 4.9: Mean eddy kinetic energy over the final four years of experiment MERC1 in a.) the upper layer and b.) the bottom layer.

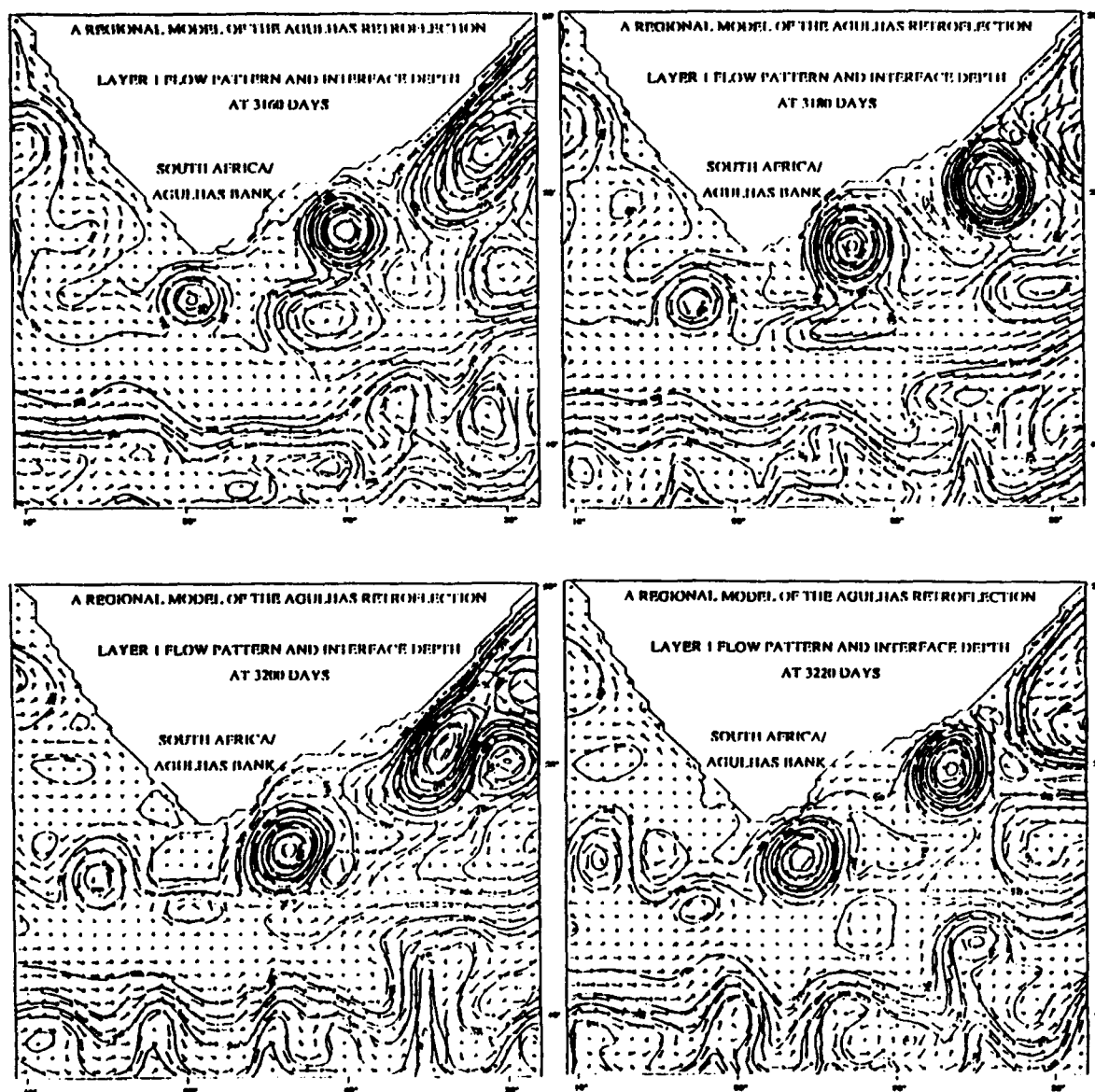


Figure 4.10: A series of instantaneous flow field and interface depth contours from experiment MERC1.

for the surfacing of coordinate surfaces and therefore will allow the thermocline to surface and outcrop.

Velocity time series have been extracted from the models for the last two years of the experiments at the points in the model corresponding to the locations of the moorings described above. From these time series we will examine the kinetic energy spectra in the model representation of the Agulhas region. In particular, we will look at the time series at the positions corresponding to mooring 838, which we refer to as mooring 5, and mooring 839, referred to as mooring 6. We should not expect that the model can produce similar kinetic energy distributions in all regions of the frequency spectrum, since the model lacks the physics to deal with the highest frequency waves, and since there is a high-frequency cutoff due to the spatial truncation imposed by discrete horizontal grid size. Additionally, since the model is forced by constant, approximate wind stress, we would also not expect to see good agreement in the extremely long period waves which could be caused by annual, or longer, variations in forcing. However, we would hope to see a range of frequencies in which the model will be able to reproduce the observed kinetic energy distributions.

Figure 4.11 shows the kinetic energy spectrum for a.) mooring 5 and b.) mooring 6. Mooring 5 exhibits energy peaks at 28 days and 80 days. Mooring 6 exhibits similar peaks and possesses more total energy overall. The moorings show high coherence (Fig. 4.11 c.) at periods around 80 days. This suggests that the model produces coherent structures at these long periods at length scales of 265 km. This is in contrast to the observations which showed low coherence at all periods at this length scale. Spectra for mooring 5 in layer 1 and layer 3 are shown in Figure 4.12. Peaks at 28 days appear in each spectrum along with secondary peaks at 80 days in layer 1 and 60 days in layer 3. Minimal vertical coherence is seen at mooring 5 between the upper and lower layers of the model. The same layout for mooring 6 is shown in figure 4.13. Again, the upper layer peak at 28 days is evident along with lower layer peaks at 30 days, 65 days, and 150 days. Coherence is low at all periods below 100 days.

It is of interest to make one additional comparison between the model and observations. The satellite altimeter measurements of Gordon and Haxby presented above provide a benchmark against which to compare Agulhas eddy tracks from the model. Unfortunately, measurements of Agulhas eddies from satellite sea surface height (SSH) data are only useful after the eddies have drifted away from the Agulhas region. While the eddies are still south of Africa, their sea surface height signal is obscured by the general variability of the Agulhas. It is only when they propagate into the South Atlantic, and their SSH signal contrasts with the waters of the eastern subtropical gyre, that they can be detected

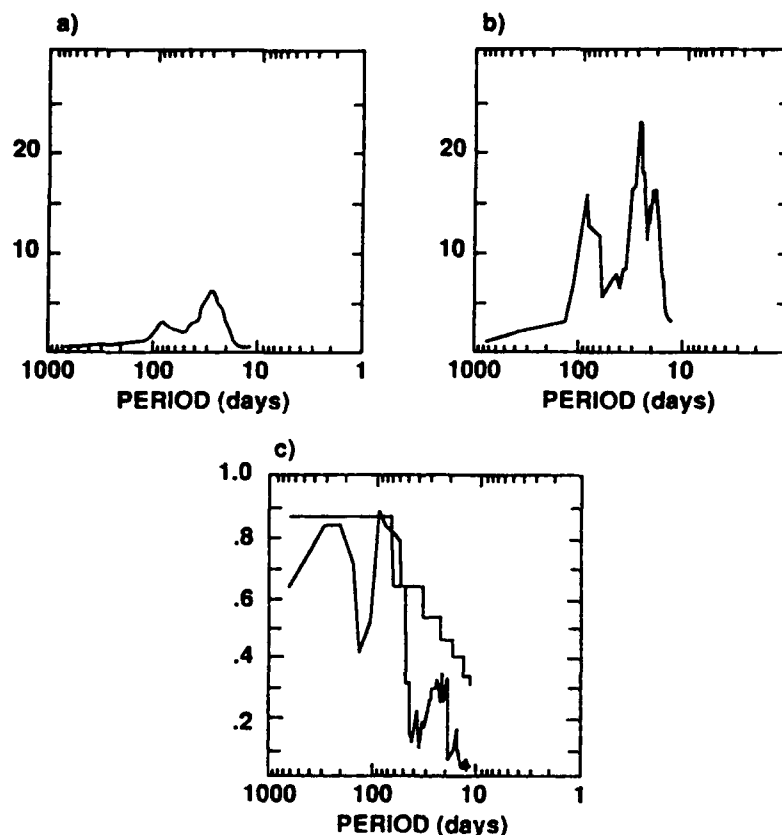


Figure 4.11: Kinetic energy spectra in layer 1 of exp. MERC1 from moorings a.) 5 and b.) 6 (units are in $10^5 \text{cm}^4 \text{sec}^{-4}$) and c.) squared coherence (confidence interval is 95 %).

by satellite altimeters. The Gordon and Haxby data show us, however, that the eddies drift generally westward or northwestward upon exiting the Agulhas region. Figure 4.14 shows the tracks of the centers of several rings formed over the last two years of experiment MERC1. It appears the model eddies follow a course consistent with the data after they enter the South Atlantic.

However, it is from these model eddy tracks that we can begin to explain the discrepancy in the mean flow vectors of MERC1 and the observations at current meters 5 and 6. Recall that Figure 4.8 shows that the model produces mean eastward flow at the moorings south of Africa, while the data show westward mean flow. By considering the tracks of the model eddies in the figure, recalling that the flow in the eddies is anticyclonic, the region to the south of the eddy centers will exhibit eastward flow most of the time. So the model eddy tracks, coupled with the mean flow data, suggest that the model forms rings which remain too close to the coast compared with the real Agulhas. The current meter mean flow vectors indicate that the center of the Agulhas eddies pass to the south of moorings 5 and 6. Consequently, the moorings are on the north side of the anticyclonic flow, directed toward the west.

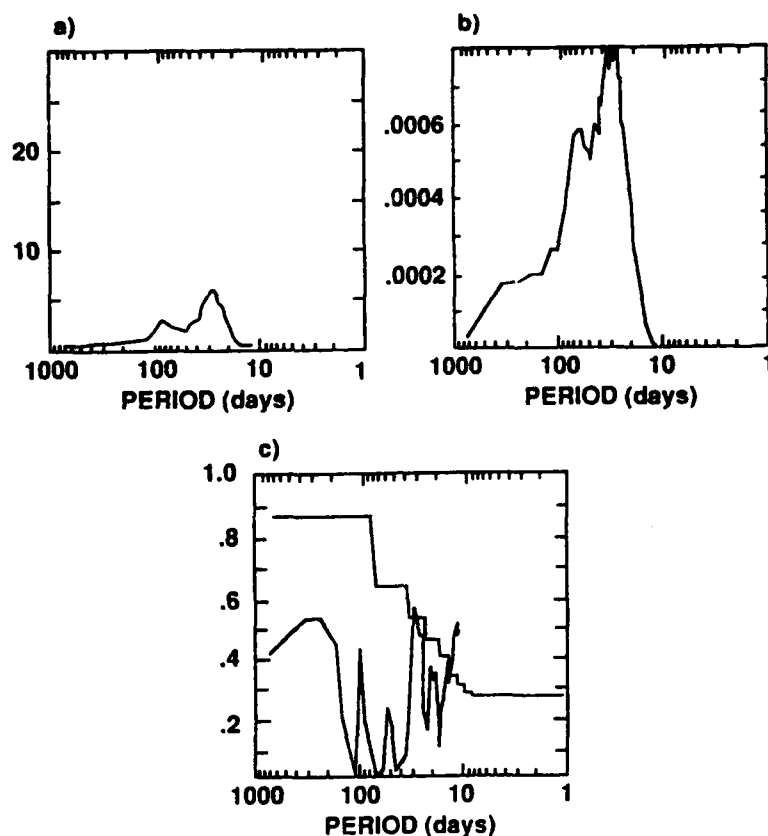


Figure 4.12: Kinetic energy spectra from exp. MERC1 mooring 5 a.) layer 1, b.) layer 3 (units are in $10^5 \text{cm}^4 \text{sec}^{-4}$) and c.) squared coherence (confidence interval is 95 %).

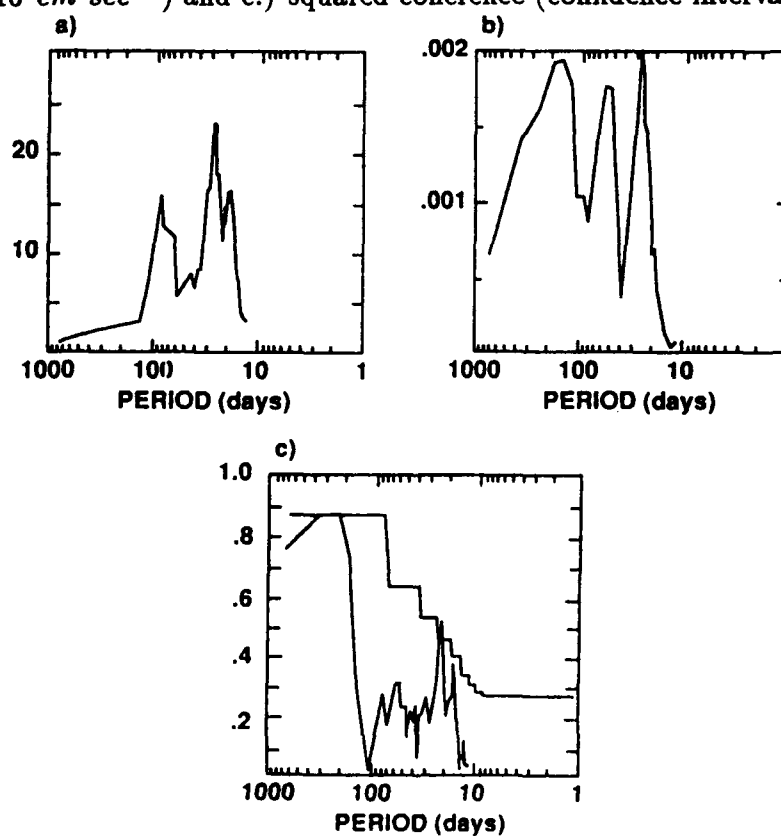


Figure 4.13: As in Figure 4.12 for mooring 6.

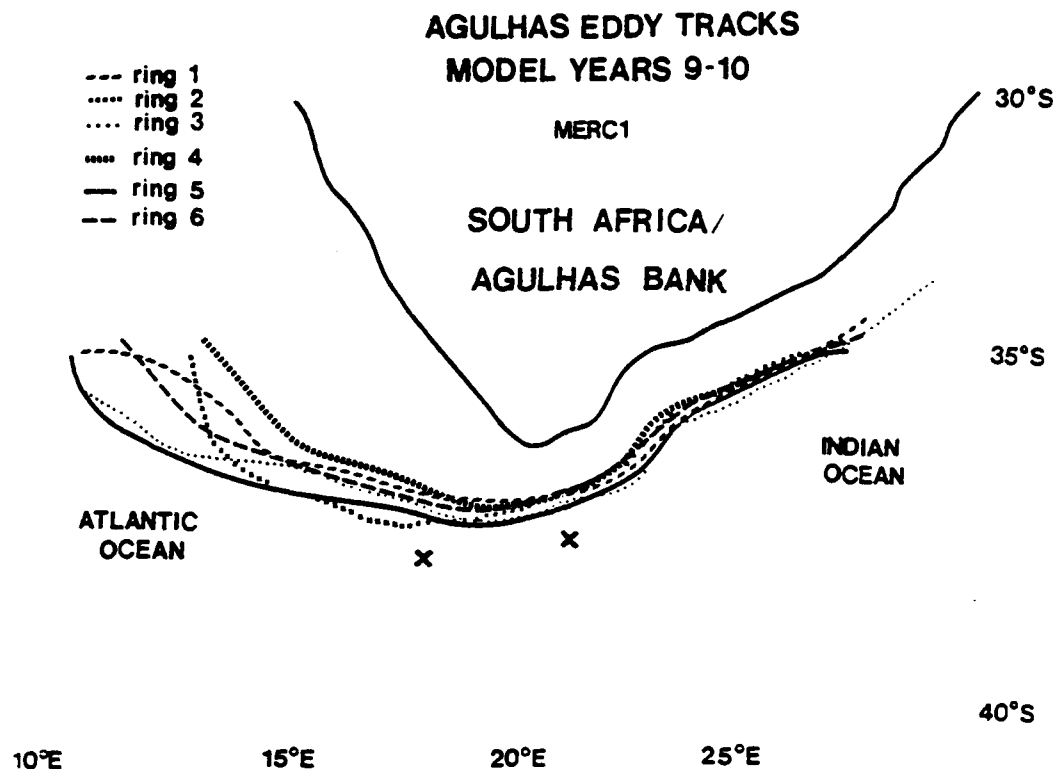


Figure 4.14: Eddy tracks during the final two years of experiment MERC1. Crosses indicate the location of moorings 5 and 6.

4.2.2 Experiment FCTMERC

Figure 4.15 shows the layer 1 and 2 mean flow pattern for FCTMERC. The strong south-westward flow in the Agulhas core in the current meter data is weaker in this experiment where velocities are less than 50 cm everywhere. Again in this experiment, the model produces weak eastward flow south of the shelf break, while the observations show westward flow in this region. From the discussion above, we expect that the eddy tracks in this model will be similar to those in MERC1. South of 40°, however, the model flow agrees well with that observed. In general, the character of the retroflection is weak in the upper layers of this experiment. The current core hugs the coastline and much of it turns around the tip of Africa and into the South Atlantic. Figure 4.16 shows a series of instantaneous flow field pictures which depict an eddy formation event in experiment FCTMERC. There are approximately 6-7 of these events per model year. The eddies are seen to begin their development in the area along the coast at 35°S and subsequently drift southwestward around the tip. This ring development is in contrast to that seen in Figure 4.10 for MERC1 where the eddies were fully developed at 35°S due to the premature retroflection of the current. This difference is strikingly evident in Figure 4.17 which shows the layer 1 eddy kinetic energy for FCTMERC. The EKE magnitude has fallen dramatically in comparison to MERC1, but now the bulk of the eddy activity occurs just southeast of the African tip.

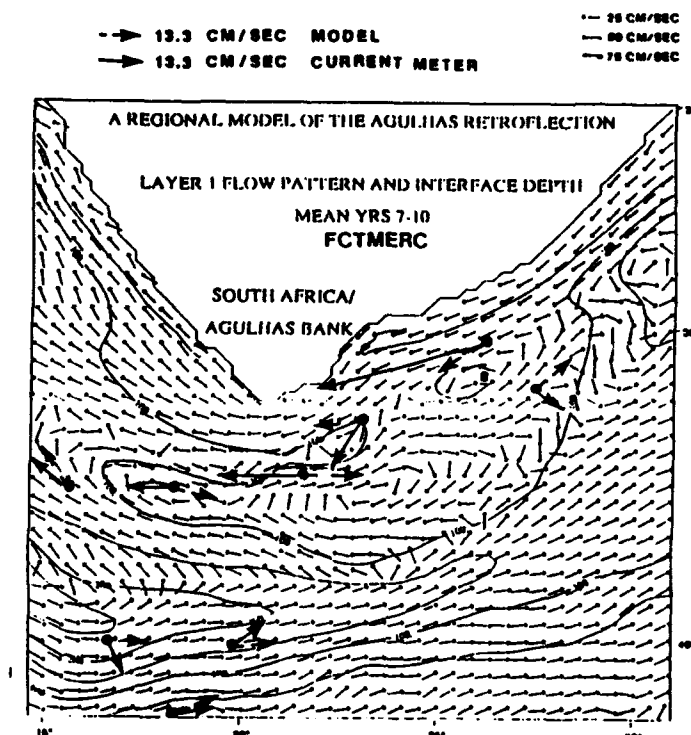


Figure 4.15: Mean flow vectors from current meter data and experiment FCTMERC. Heavy solid arrows depict current meter data. Heavy dashed arrows depict model data at the current meter location. Small arrows are model velocities. Contour lines indicate model mean interface depth in meters.

In fact, the location of the maximum EKE values, along $37^{\circ}S$, agrees well with location of the current meter derived maximum.

These contrasting results between FCTMERC with MERC1 point out some important differences between the two model experiments. First, the five layer model shows weaker flow in the upper layers than the three layer model. We have seen this above in Chapter 3 where we concluded that the decrease in static stability in the upper ocean leads to a faster transition of the flow to a baroclinically unstable regime in which more of the energy is pumped into the lower layers. It appears that to better attempt to simulate the observed flow in the Agulhas region, a five layer model with mean stratification more resembling that of MERC1 should be used since this presumably would prevent this early onset of baroclinic instability and keep much of the energy provided by the wind trapped in the upper layers.

The more surprising result though, is the tendency for the current in the five layer case to stay closer to the African coast for a longer time, not separating as in the earlier case. This leads to the formation of rings in a position more supported by the data in the real Agulhas. The reason for this difference is attributable to the ability of the five layer model to support outcropping coordinate interfaces. Figure 4.18 shows the mean layer thickness

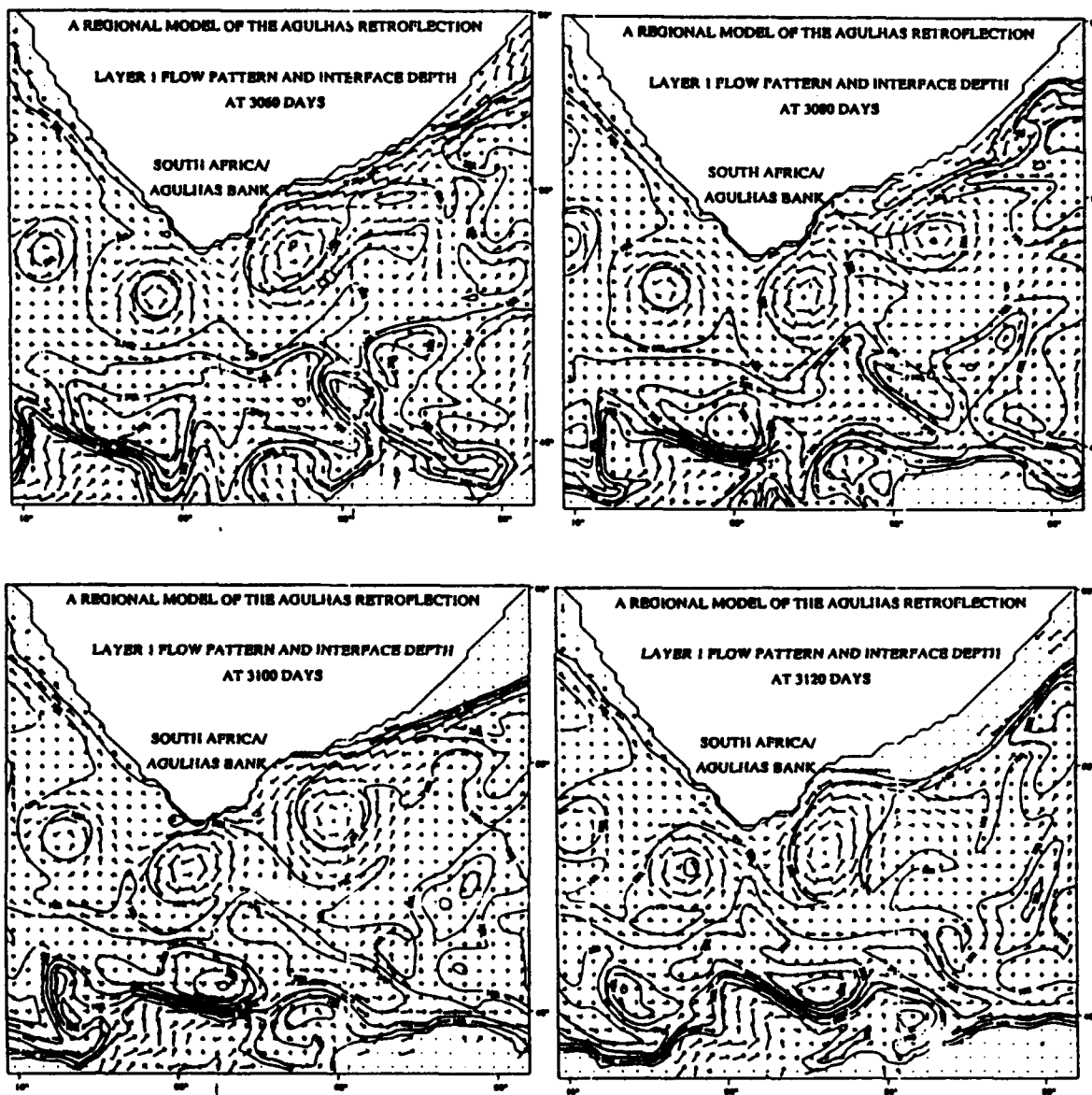


Figure 4.16: A series of instantaneous flow field and interface depth contours from experiment FCTMERC.

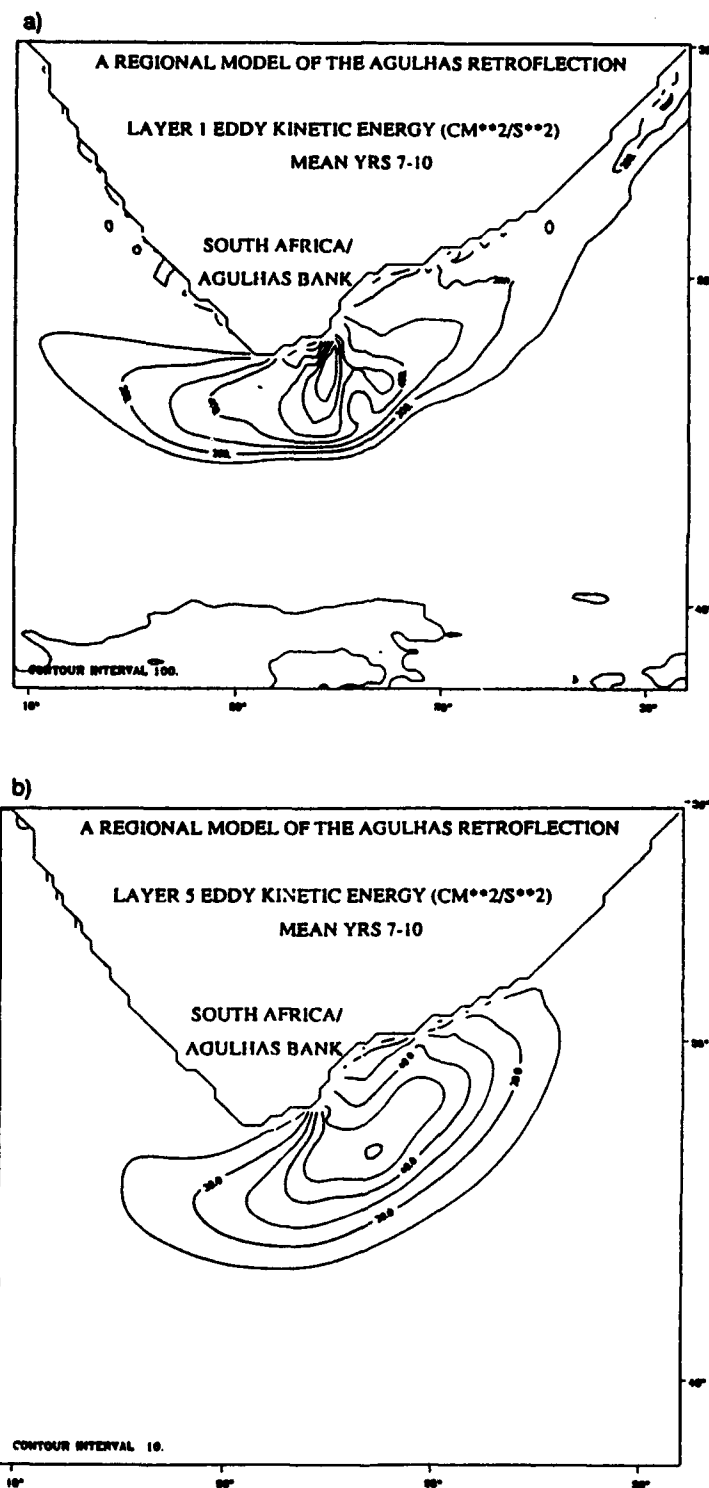


Figure 4.17: Mean eddy kinetic energy over the final four years of experiment FCTMERC in a.) the upper layer and b.) the bottom layer.

for both experiments over the last 4 years of each experiment. The three layer case shows a layer thickness pattern in the Indian Ocean basin consistent with a large scale Sverdrup gyre feeding into the Agulhas system along the African western boundary. The upper layer in MERC1 is depressed to deeper than 600 m directly to the east of the continent. Also evident is the retroflecting nature of the current along the coast. In contrast, the mean layer thickness pattern in FCTMERC shows that, in much of the Indian basin, layer 1 is less than 50 m from the surface. In essence, much of the Indian basin has "dried up". This situation was discussed briefly in Chapter 3 above and it is evident that some type of quasi-thermodynamic forcing could be incorporated in a model of this type to avoid this. In this way, water would be allowed to sink from layer 1 to lower layers in the southwestern South Atlantic where there is evidence of convective mixing (Olson *et al.* 1988; Fine *et al.*, 1988) and would be allowed to return to the upper layer again in the Indian ocean. Nevertheless, this outcropping phenomenon appears to have a profound effect on the Agulhas system. Top layer water enters the boundary current only south of 30° S and flows down the coast without separating as in the three layer case. It appears from Figure 4.16 that ring development occurs as the current flows out of the concave feature of the coastal geometry at around 36° S.

To obtain an idea of the amount of water lost in the upper layer of the experiment, the volume of water in the Indian Ocean east of 20° E was calculated at the beginning of the experiment and at one year intervals. This calculation gives us the opportunity to assess how much of the upper layer is transferred into the Atlantic Ocean during the integration. It also allows us to estimate the volume flux of upper ocean water around the tip of Africa. As discussed above, Gordon (1986) has proposed that the Agulhas may provide the warm water to the Atlantic Ocean needed to balance the export of North Atlantic Deep Water (NADW) formed at high latitudes. Our calculation will provide an estimate of purely wind-driven interbasin exchange. Over the entire ten year integration, the average net volume flux of Indian Ocean water which gets around the African continent in the upper layer is 1.1 Sv. Layers two and three lose water to the Atlantic also bringing the total net volume flux to 1.9 Sv. Gordon has estimated that approximately 7 Sv would be necessary to balance the NADW export. His theory also includes inflow from the Pacific to the Indian Ocean through Indonesia, which our model does not include because of its closed boundaries.

Just as we compared spectral characteristics of MERC1 with those of moorings 5 and 6, we will compare spectra from FCTMERC at those points. Figure 4.19 shows the spectra in layer two at moorings 5 and 6 along with the squared coherence between the two

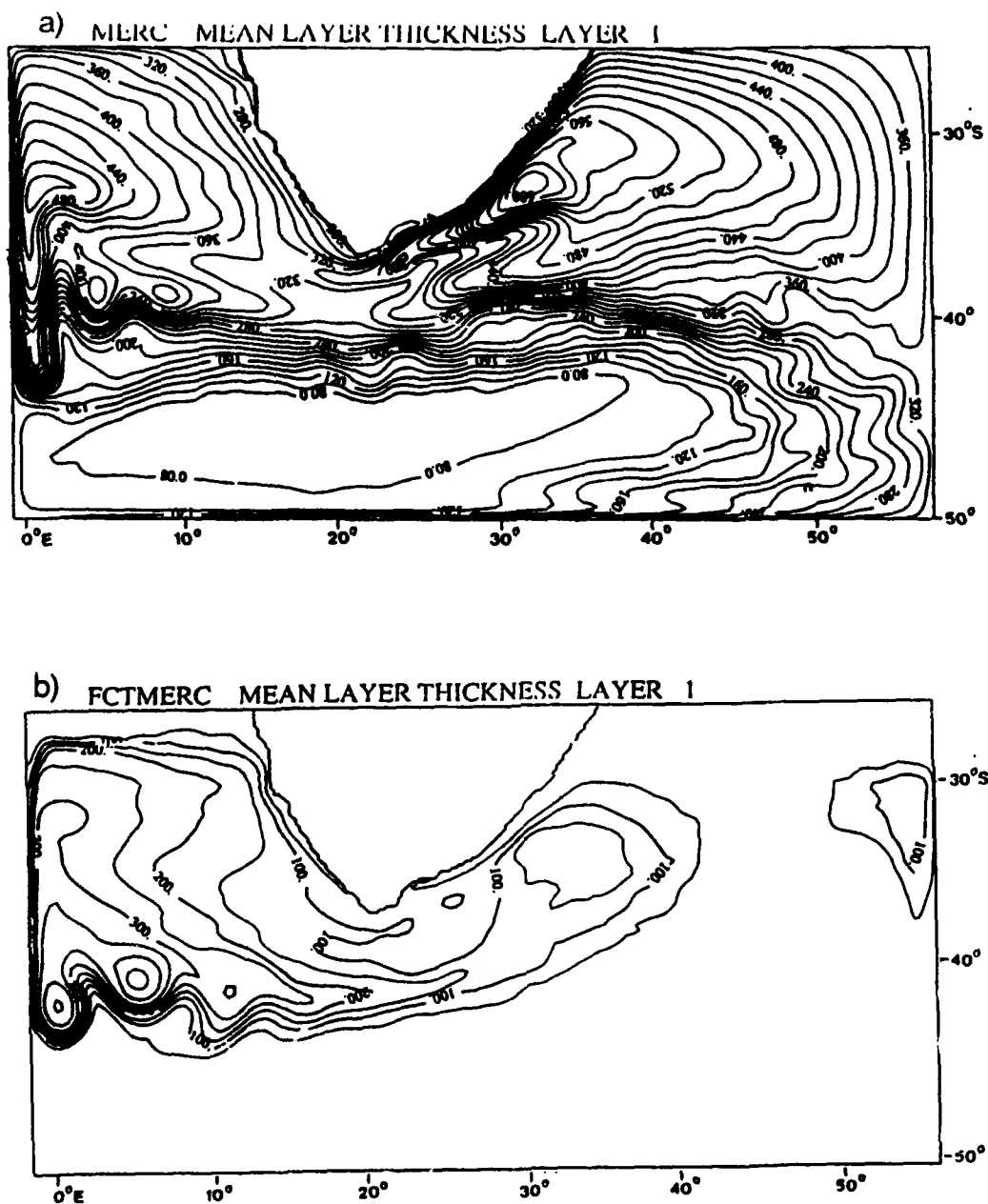


Figure 4.18: Mean layer thickness in entire domain for a.) experiment MERC1 and b.) experiment FCTMERC. Units are in meters.

series. Layer two spectra were chosen to correspond roughly with the nominal depth of the moorings which was approximately 200 m. Since layer one of the model was only about 100 m thick in the mooring region, layer two spectra were used. Immediately obvious in the figure is that FCTMERC is less energetic than either the observations (Fig. 4.3) or MERC1 (Fig. 4.11). Also evident at both moorings is that FCTMERC tends to produce sharper peaks than observed or the previous model, although the energy appears to be distributed in the same part of the spectrum. In fact, as we proceed from the FCTMERC spectra, through the MERC1 spectra, to the observed spectra, each successive step appears as though it is a smoothed version of the one previous to it. Perhaps most striking is that in FCTMERC the squared coherence is very high at all periods between 10 days and 100 days. This suggests that FCTMERC produces scales longer than 265 km. These results suggest that the model solutions are increasingly less turbulent than the real ocean. Instead of smoothly distributing energy over a range of frequencies, energy is deposited discretely into coherent structures. In both simulations this is a result of the lack of small scale features in the model due to spatial truncation. This phenomenon is enhanced here in FCTMERC because the model tends to produce more barotropic features. This results from the increased pumping of energy into the deeper ocean as discussed above. Figure 4.20 shows the spectra from mooring 5 in layers two and five to illustrate the increased barotropic nature of the flow. We see high coherence at all periods between 10 and 100 days. Figure 4.21 shows the same situation for mooring 6. High vertical coherence in the spectra from FCTMERC is consistent with increased vertical energy transfer in the model with decreased upper ocean static stability and suggests that the model produces larger eddies even in the deeper layers.

Figure 4.22 shows the tracks of the eddies produced in experiment FCTMERC. Three things are apparent in this figure. First, the eddies are seen to form south of 35°S . This is in contrast to MERC1 (Fig. 4.14) where the rings formed north of 35°S . Secondly, the rings lose their appearance sooner than in MERC1. This is because the rings start out weaker in the upper layers and are therefore dissipated more quickly in FCTMERC. The lateral viscosity coefficient is somewhat larger in FCTMERC as discussed in the experimental design section. This may contribute to the quicker dissipation of the eddies. Finally, there is not as much spread in the tracks in FCTMERC as there was in MERC1, all of the eddies tend to take almost the same trajectory. Again in FCTMERC however, the eddy tracks suggest that the rings remain too close to the coast and are responsible for the discrepancy in the mean flow between the model and the observations at moorings 5 and 6 (Fig. 4.15).

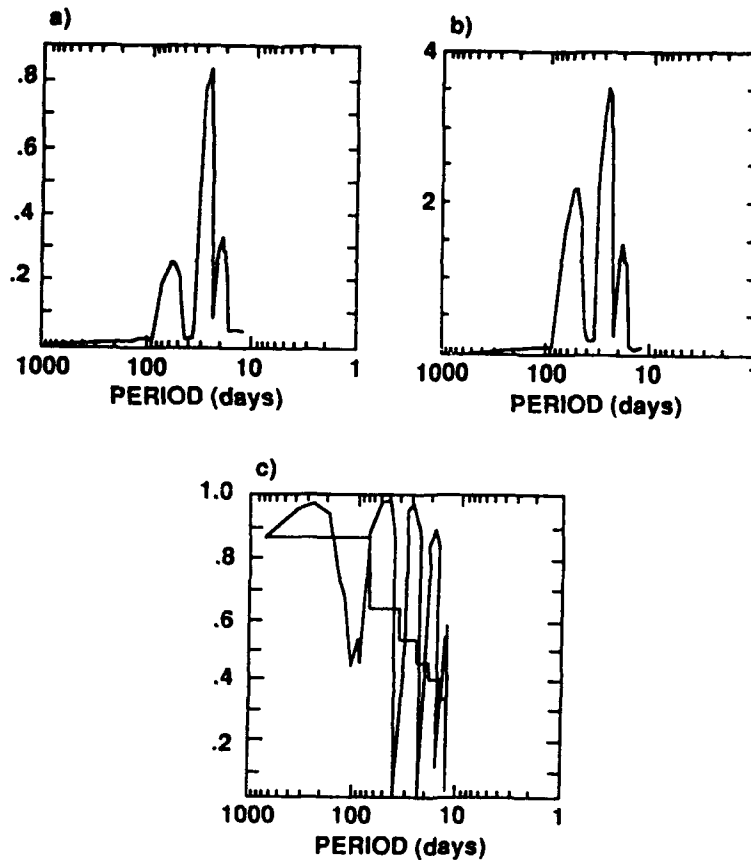


Figure 4.19: Kinetic energy spectra in layer 1 of exp. FCTMERC from moorings a.) 5 and b.) 6 (units are in $10^5 \text{cm}^4 \text{sec}^{-4}$) and c.) squared coherence (confidence interval is 95 %).

4.3 Summary

The Agulhas model was modified to incorporate an increased basin size and a more realistic coastal geometry configuration in an effort to compare the model results with results of recently gathered observations in the Agulhas region.

First the observations were described. Observations include a set of current meter mooring time series of velocity taken over a two year time period south of the African continent, and Agulhas eddy trajectories derived from satellite sea surface height measurements. Mean flow vectors from the current meter time series show strong flow along the Agulhas shelf break and a mean retroflection generally south of 40°S . Horizontal plots of eddy kinetic energy derived from the time series show maxima of EKE in both the upper and lower ocean along 37°S in the region of Agulhas eddy formation. Kinetic energy spectra derived from the observations in the region of maximum EKE show broad peaks at 37 day periods and low coherence, suggesting length scales less than 265 km and an eddy shedding frequency of five per year. Agulhas eddy tracks derived from SSH measurements show eddies exiting the Agulhas region and drifting into the South Atlantic Ocean.

A large domain, three-layer experiment (MERC1) which is similar to experiment E11

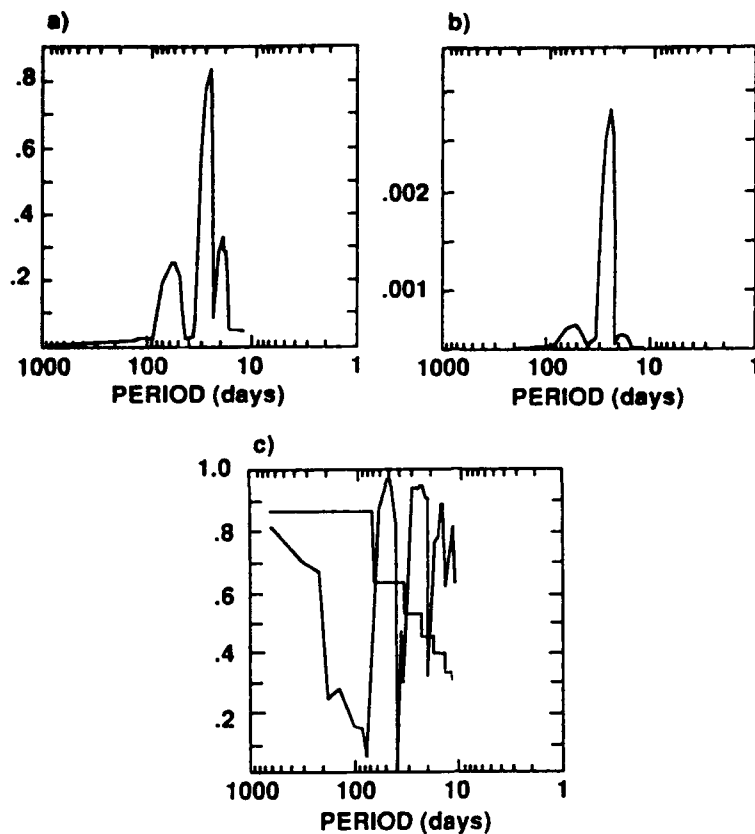


Figure 4.20: Kinetic energy spectra from exp. FCTMERC mooring 5 a.) layer 1, b.) layer 5 (units are in $10^5 \text{cm}^4 \text{sec}^{-4}$) and c.) squared coherence (confidence interval is 95 %).

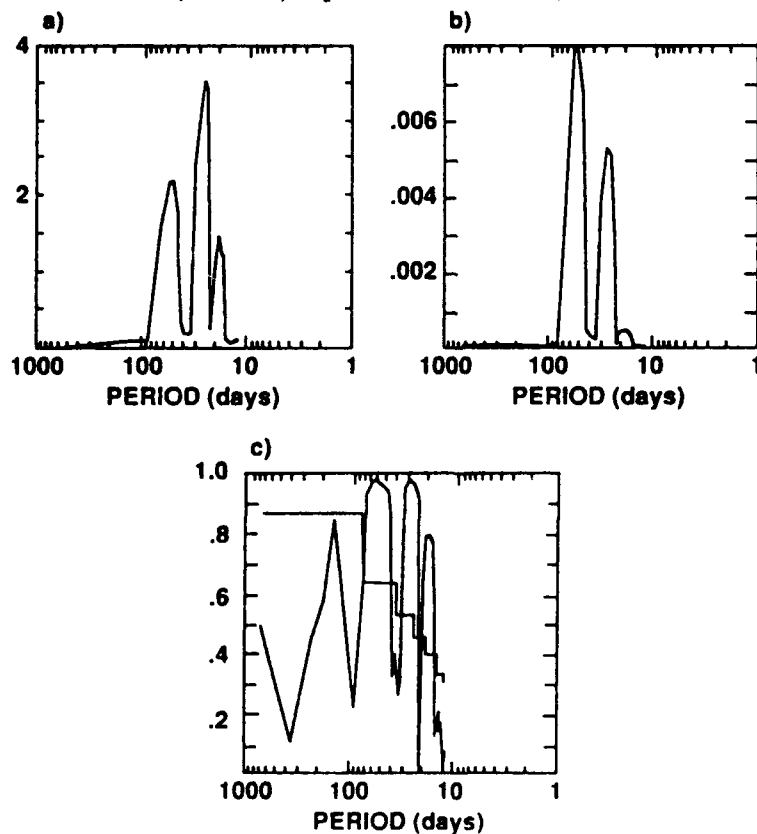


Figure 4.21: As in Figure 4.20 for mooring 6.

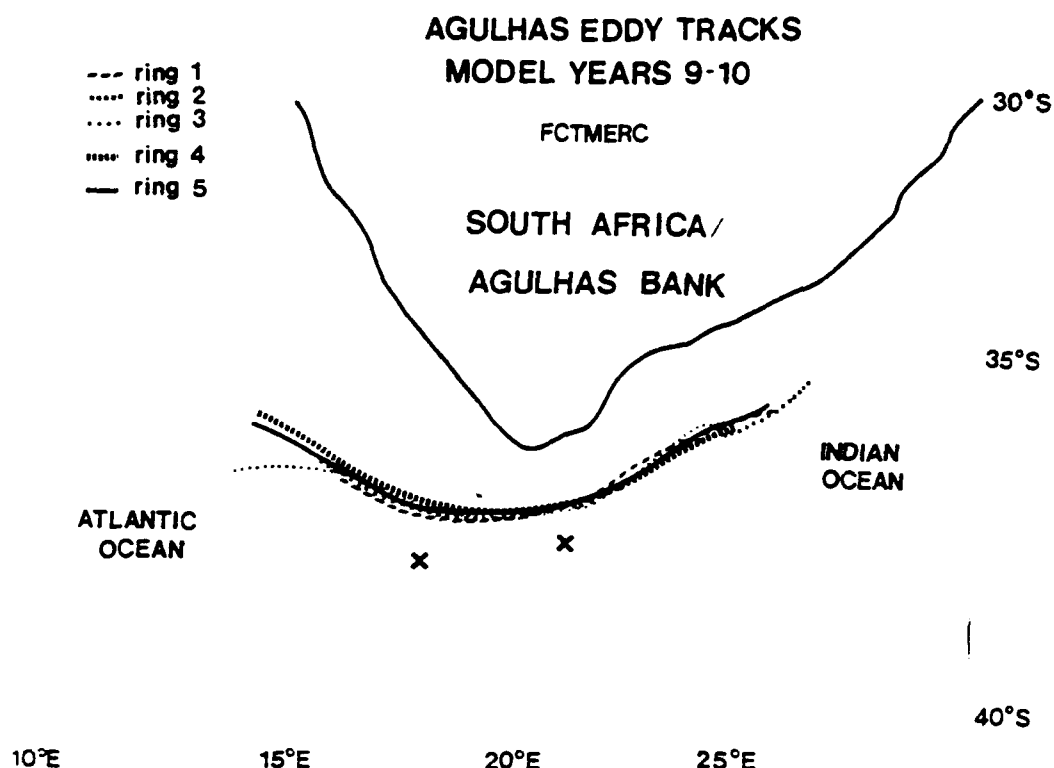


Figure 4.22: Eddy tracks during the final two years of experiment FCTMERC. Crosses indicate the location of moorings 5 and 6.

described in Chapter 3 was compared to the observations. In this experiment, the Agulhas separates from the coast well north of the tip of Africa, undergoing a retroflection and ring formation in the process. Consequently, the regions of high EKE differ from those observed in location, although the model produces EKE of the observed magnitude. Kinetic energy spectra from the model at points corresponding to the moorings show energy peaks of 28 and 80 days. The coherence is low, suggesting that the model is producing scales of less than 265 km. Ring tracks, coupled with the mean flow data, suggest that the rings formed in the model remain too close to the coast when compared to the real eddies. They drift westward or northwestward upon entering the South Atlantic, consistent with the observations.

A five-layer experiment (FCTMERC) incorporating the Flux Corrected Transport (FCT) algorithm which allows outcropping of coordinate surfaces was then compared to the observations. This experiment corresponds to experiment FCT4 in Chapter 3. In this experiment, the overall Agulhas is weaker, especially in the upper layers, but the current core remains close to the coast until it reaches the African tip where it separates and retroflects. In this case, rings are formed farther down the coast toward the tip. This is evident in the EKE distribution in which maximum EKE is located along 37° S, in a position much closer to the observed than in experiment MERC1. The kinetic energy

spectra from FCTMERC show sharper peaks than in MERC1 or the observations. The coherence is high through the entire range of periods, suggesting that FCTMERC produces longer scales than MERC1. Weakened upper ocean static stability in FCTMERC results in an increased transfer of energy from the upper ocean to the deeper layers as discussed in Chapter 3. This is manifest as high vertical coherence in the FCTMERC time series. The solution is overall less turbulent than reality with energy being distributed discretely into coherent structures. Finally, ring tracks in this experiment are very similar to those in MERC1.

Chapter 5

Discussion

A numerical modeling study of the Agulhas Current using a primitive equation, isopycnic coordinate model was carried out. Our first goal was to investigate the effect of increased vertical resolution and varying upper ocean static stability on the current system in general and the rings in particular. Secondly, using a basin which is four times larger and a more realistic coastal geometry configuration, we compared the model results with observations recently collected in the Agulhas region. A series of five experiments were performed and compared to carry out the first goal. For the second part of the research, two experiments were performed.

5.1 Effects of increased vertical resolution

The model used in the first part of this study is a pure isopycnic model which handles outcropping isopycnal coordinate surfaces in a numerically trouble-free fashion. To encourage isopycnal outcropping, the upper ocean static stability was reduced. This allowed the density surfaces to deform more easily. The major effect of this change was to reduce the total energy of the simulations. As the density surfaces deformed, vertical shear was built up more quickly and baroclinic instabilities grew faster. Thus much of the wind energy, trapped in the upper ocean in earlier experiments, was pumped downward in the new experiments resulting in less energetic upper layers and increasingly more energetic intermediate and lower layers. The overall decrease in energy of the experiments with increased vertical resolution suggests that the instabilities were somewhat better resolved, allowing dissipation process active in the model, in particular lateral viscosity, to better dissipate energy input by the wind.

The effects of the changes in vertical resolution and static stability on the Agulhas

retroflexion was to move the mean Agulhas recirculation region to a more southwestward position to a location more towards the tip of the African continent. This corresponds to Agulhas ring formation further down the coast and in a position more consistent with that seen in Agulhas eddy observations.

Finally, the incorporation of outcropping coordinate surfaces leads to a unique problem in the model whereby fluid in the upper layer which flows from the Indian Ocean around the tip of Africa becomes trapped in the Atlantic. This is because it is precluded from reentering the Indian Ocean due to the outcropping of isopycnals in the subtropical convergence zone and the subsequent lack of an upper layer south of that region. In the real ocean, water entering the South Atlantic basin is cooled by the high heat fluxes in the region. This fluid sinks and is therefore able to return to the Indian Ocean as more dense water at a deeper level. Obviously, the exclusion of explicit thermodynamic forcing in the present model is a shortcoming which must be addressed in the future.

5.2 Comparison with observations

The second part of this work was aimed at quantitatively comparing a set of more realistic simulations with some observations taken in the Agulhas region. The main areas of investigation were 1) a comparison of the mean flow of the model and observations, 2) how the model distributes energy, both spatially and temporally, compared with the real ocean, and 3) how the model eddy trajectories compare to eddy tracks of real Agulhas eddies. To make the model more realistic, the basin dimensions were doubled, leading to a basin with four times the area of the previous domain. Additionally, the African coastal geometry was made to more resemble the actual Agulhas shelf break configuration. First, a three layer model was run in this domain, and then a five layer simulation was carried out.

The three layer model produced mean velocities in the Agulhas current core which are very similar to those observed through direct current meter measurements. The character of the modeled retroflexion however, differs somewhat from the observations. The model Agulhas separates from the coast well up the African shelf break, quite a bit north of the tip of the continent. This leads to a premature retroflexion and the formation of eddies up the coast. As a result, comparisons of eddy kinetic energy from the model and observations show a discrepancy in the location of maximum EKE both in the upper and lower ocean. Although the model does produce eddy kinetic energy of the same magnitude as seen in the observations, the EKE maxima are displaced up the coast relative to the observations.

Comparison of kinetic energy spectra show that the model represents the mesoscale

features of the ocean rather well. The energy peaks occur in essentially the same portion of the spectrum, suggesting that the model is simulating the frequency of Agulhas ring formation correctly. However, the kinetic energy spectra suggest that the model solutions are less turbulent than the real ocean. This is to be expected since the model lacks the proper representation of the sub-grid scale processes present in the ocean.

Ring trajectories, coupled with the mean flow data, show that the model forms rings which are too close to the African coast as they drift into the South Atlantic. Once into the Atlantic however, the rings drift westward or northwestward as observed.

In general, the changes which appear in the five layer model run in the larger basin are consistent with the results arrived at in the investigation of increased vertical resolution. The upper ocean is less energetic and consequently, upper ocean mean velocities are somewhat weaker than those seen in the current meter measurements. The character of the retroflexion is changed however, from the premature retroflexion discussed above, to a current core that hugs the African coast until it reaches the tip of the continent where it separates and retroflects. This leads to horizontal distributions of eddy kinetic energy which compare better in location to those observed while the magnitude of the EKE is somewhat smaller. One explanation for the change in the nature of the retroflexion is the fact that the outcropping upper layer in the Indian Ocean results in the southwestward displacement of the Agulhas recirculation. This in turn results in a current core which remains close to the coast until reaching a higher latitude.

Spectral characteristics of the five layer experiment are similar to those of the three layer experiment. The decreased turbulence in the model is even more defined in the five layer experiment, however. The spectral peaks are very sharp, indicating that the model is distributing energy discretely into coherent structures. This is a result of the pumping of energy into the deep ocean and subsequent development of more barotropic features in the model.

In the five layer experiment, the ring tracks again suggest that the model eddies drift too close to the African coast. In addition, the eddies cannot be tracked as far into the Atlantic in this experiment. This is because they start out less energetic and the viscosity in the model deteriorates them more quickly. Possibly contributing to this is the fact that the viscosity was increased slightly in the five layer experiment to correct a problem with numerical instability.

5.3 Concluding Remarks

This work represents an increase in complexity of regional models used in the study of ocean currents in general and the Agulhas current in particular. Whereas earlier works were aimed at isolating and identifying the physical mechanisms at work ocean circulation, we have concentrated here on the ability of numerical models to simulate the flows of the real ocean. We still lack some important aspects of realism, including a fully realistic domain size, thermodynamics, variable wind forcing, and bottom topography. Nevertheless, it is important to assess the ability of such models by comparing their results with observations.

In general, our models produce eddy kinetic energy of the approximate magnitude of the real ocean. The energy is distributed fairly well in phase space, although the solutions display less turbulence than reality. The appearance of a problem concerning the loss of water in the Indian Ocean to the Atlantic in the experiment with isopycnal outcropping suggests that some form of thermodynamics should be incorporated in a model of this type.

As the oceanographic community draws closer to the goal of global ocean simulation and forecasting the kind of studies carried out here will be important in both assessing the ability of the models to simulate the ocean, and in pointing out deficiencies in the models. This can ultimately lead to the development of better techniques with which to improve the quality of model simulations for forecasting.

Appendix A

Wind Stress Application

The wind stress is applied as a body force over a layer but is assumed for the purpose of distribution among layers to decrease linearly from a maximum at the surface to zero at some specified depth. Thus, any layer which rises to within this depth will receive a portion of the wind forcing. To see how the wind stress is distributed among layers, consider the momentum equation (2.1) applied to each layer, including only the acceleration and wind stress terms (only the u-equation is necessary since we only apply a zonal wind stress in this model):

$$\frac{\partial u_k}{\partial t} + \dots = \dots + \alpha \frac{\partial \tau_k}{\partial z_k} + \dots \quad (\text{A.1})$$

For our purposes, we would like to transform from vertical coordinates to pressure coordinates which we can do via the hydrostatic equation:

$$\frac{\partial p}{\partial z} = \frac{g}{\alpha}. \quad (\text{A.2})$$

If we rewrite the momentum equation using this transformation and in finite difference form,

$$\frac{\Delta u_k}{\Delta t} + \dots = \dots + g \frac{\Delta \tau_k}{\Delta p_k} + \dots \quad (\text{A.3})$$

The wind stress profile is defined as:

$$\tau_k = \tau_0 \left(1 - \frac{p_k}{p_{max}} \right) \quad (\text{A.4})$$

and all other interfacial stresses are equal to zero. This definition provides that if any interface rises to within p_{max} , it will receive a portion of wind stress which is linearly related to its depth.

Figure A a.) shows the initial configuration for a three layer model, b.) shows a possible situation later in the integration where the interfaces have risen to within p_{max} . Note that

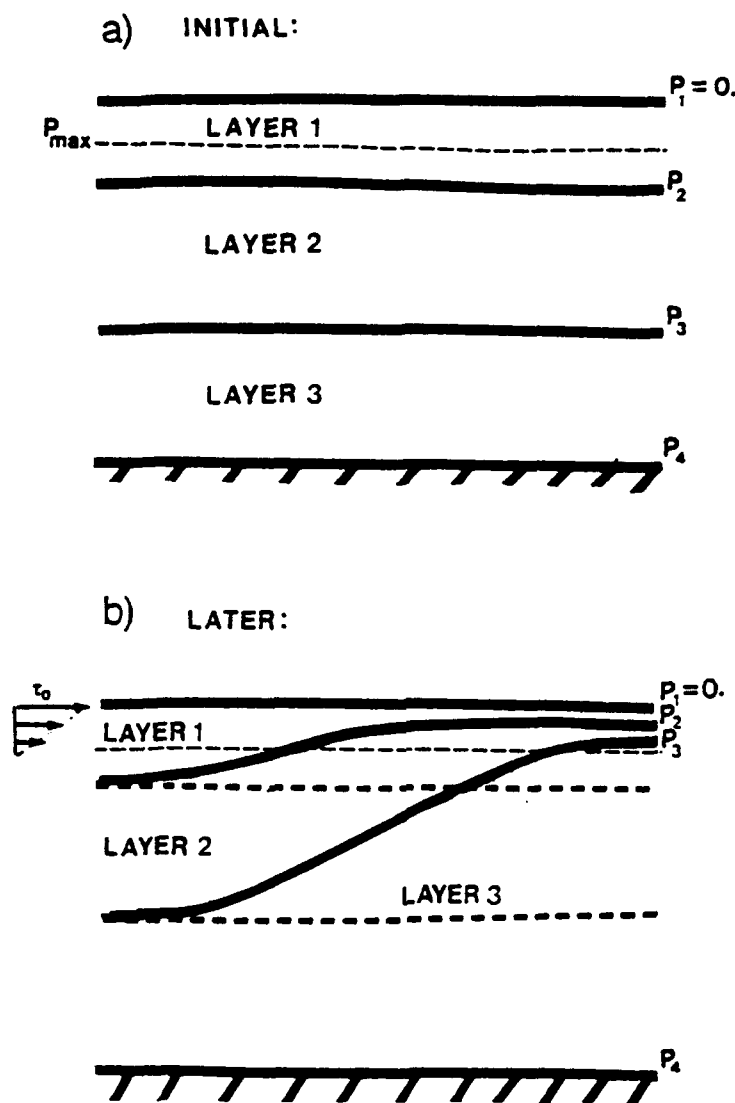


Figure A.1: a.) Initial configuration for a three layer model. b.) Possible configuration of model after integration has proceeded for some time. Wind stress profile is at left. (Figure not to scale.)

the pressure at the surface, actually the rigid lid pressure, can be set to zero since it is approximately three orders of magnitude less than the pressures at the other interfaces. As the integration of the model proceeds, a layer may be either entirely below the maximum wind forcing depth, as is the case for layers two and three in figure A a.), partially below the maximum wind forcing depth, such as layer one in the initial configuration, or entirely contained within the wind forcing depth, such as layer two in figure A b). We will examine the three cases.

a.) Case 1

If a layer is completely below the maximum wind stress depth, the contribution of the wind stress to the acceleration in the momentum equation for that layer becomes:

$$g \frac{\Delta \tau_k}{\Delta p_k} = g \frac{\tau_k - \tau_{k+1}}{p_{k+1} - p_k} = 0 \quad (\text{A.5})$$

which is correct because the interfacial stresses are zero in the absence of wind stress.

b.) Case 2

If a layer is partially below the wind forcing depth, then A.5 becomes:

$$g \frac{\tau_k}{p_{k+1} - p_k} \quad (\text{A.6})$$

since then $\tau_{k+1} = 0$ because p_{k+1} is below the wind stress depth. Then, substituting A.4 we have:

$$g \frac{\tau_0 (1 - \frac{p_k}{p_{max}})}{p_{k+1} - p_k} \quad (\text{A.7})$$

which becomes:

$$\frac{g \tau_0}{p_{max}} \left(\frac{p_{max} - p_k}{p_{k+1} - p_k} \right) \quad (\text{A.8})$$

As an example, for layer one in figure A, $p_1 = 0$ so A.8 reduces to:

$$\frac{g \tau_0}{p_2} \quad (\text{A.9})$$

c.) Case 3

For a layer which completely exists within the maximum wind stress depth, A.5 becomes:

$$g \left(\frac{\tau_0 (1 - \frac{p_k}{p_{max}}) - \tau_0 (1 - \frac{p_{k+1}}{p_{max}})}{p_{k+1} - p_k} \right) \quad (\text{A.10})$$

which reduces to:

$$\frac{g \tau_0}{p_{max}} \left(\frac{p_{k+1} - p_k}{p_{k+1} - p_k} \right) = \frac{g \tau_0}{p_{max}} \quad (\text{A.11})$$

This amounts to constant wind stress forcing for any layer entirely existing within the maximum wind forcing depth.

In the model, this scheme is applied by computing:

$$\frac{g\tau_0}{p_{max}} \left[\frac{\min(p_{k+1}, p_{max}) - \min(p_k, p_{max})}{p_{k+1} - p_k} \right] \quad (A.12)$$

at each point for each layer each time step.

Any scheme which distributes wind stress among layers must still provide vertically integrated transport consistent with the Sverdrup formula. To see that this scheme correctly prescribes the vertically integrated transport in the model we will compute the vertically integrated Sverdrup transport for our example three layer case. In the present model we apply only a zonal wind stress, the momentum equations in each layer, retaining only the Coriolis, wind stress, and pressure gradient terms, are as follows:

$$-f\rho v_k = \frac{\partial \tau_{xk}}{\partial z} - \frac{\partial p_k}{\partial x} \quad (A.13)$$

$$f\rho u_k = -\frac{\partial p_k}{\partial y} \quad (A.14)$$

In each layer we integrate vertically using the hydrostatic equation,

$$-f\rho v_k \left(\frac{\alpha}{g} \Delta p_k \right) = \frac{\partial \tau_{xk}}{\partial z} \left(\frac{\alpha}{g} \Delta p_k \right) - \frac{\partial p_k}{\partial x} \left(\frac{\alpha}{g} \Delta p_k \right) \quad (A.15)$$

$$f\rho u_k \left(\frac{\alpha}{g} \Delta p_k \right) = -\frac{\partial p_k}{\partial y} \left(\frac{\alpha}{g} \Delta p_k \right) \quad (A.16)$$

Taking the curl of these equations, we arrive at the Sverdrup balance in each layer:

$$\beta v_k \frac{\Delta p_k}{g} = -\frac{\partial}{\partial y} \left(\frac{\partial \tau_{xk}}{\partial z} \cdot \frac{\alpha}{g} \Delta p_k \right) \quad (A.17)$$

Summing this over the number of layers:

$$\sum_{k=1}^N \left[\beta v_k \frac{\Delta p_k}{g} \right] = -\frac{\partial}{\partial y} \left[\sum_{k=1}^N \left(\frac{\partial \tau_{xk}}{\partial z} \cdot \frac{\alpha}{g} \Delta p_k \right) \right] \quad (A.18)$$

The left hand side is βM_y where M_y is the vertically integrated transport. What remains is to reduce the right hand side. Using our three layer example, and substituting from above, the right hand side becomes:

$$-\frac{\partial}{\partial y} \left[\frac{g\tau_0}{p_{max}} \frac{\alpha}{g} (p_2 - p_1) + \frac{g\tau_0}{p_{max}} \frac{\alpha}{g} (p_3 - p_2) + \frac{g\tau_0}{p_{max}} \frac{\alpha}{g} \left(\frac{p_{max} - p_3}{p_4 - p_3} \right) (p_4 - p_3) \right] \quad (A.19)$$

$$= -\frac{\partial}{\partial y} \left[\frac{g\tau_0}{\alpha p_{max}} \frac{\alpha}{g} (p_2 - p_1 + p_3 - p_2 + p_{max} - p_3) \right] \quad (A.20)$$

Which reduces to $-\frac{\partial \tau_0}{\partial y}$. So combining the left hand side with the right hand side we arrive at the Sverdrup relation:

$$\beta M_y = -\frac{\partial \tau_0}{\partial y} \quad (A.21)$$

References

- Arakawa, A. and Lamb, V.R., 1981. A potential enstrophy and energy conserving scheme for the shallow water equations. *Mon. Wea. Rev.*, **109**, 18-36.
- Batteen, M. L. and Han, Y.-J., 1981. On the computational noise of finite-difference schemes used in ocean models. *Tellus*, **33**, 387-396.
- Bennett, S.L., 1988. Where three oceans meet: the Agulhas Retroflection region. Doctoral dissertation, Woods Hole Oceanographic Institution/Massachusetts Institute of Technology, 367 pp.
- Bleck, R. and Boudra, D.B., 1981. Initial testing of a numerical ocean circulation model using a hybrid (quasi-isopycnic) vertical coordinate. *J. Phys. Oceanogr.*, **11**, 755-770.
- Bleck, R. and Boudra, D.B., 1986. Wind-driven spin-up in eddy-resolving ocean models formulated in isobaric and isopycnic coordinates. *J. Geophys. Res.*, **91**(C6), 7611-7621.
- Boris, J.P. and Book, D.L., 1973. Flux-corrected transport, I, SHASTA, a fluid transport algorithm that works. *J. Computat. Phys.*, **11**, 38-69.
- Boudra, D.B. and de Ruijter, W.P.M., 1986. The wind-driven circulation of the South Atlantic-Indian Ocean. II: Experiments using a multi-layer numerical model. *Deep-Sea Res.*, **33**, 447-482.
- Boudra, D.B. and Chassignet, E.P., 1988. Dynamics of Agulhas Retroflection and ring formation in a numerical model. I: The vorticity balance. *J. Phys. Oceanogr.*, **18**, 280-303.
- Boudra, D.B., Maillet, K.A., and Chassignet, E.P., 1989. Numerical modeling of Agulhas Retroflection and ring formation with isopycnal outcropping. In *Mesoscale Synoptic*

- Coherent Structures in Geophysical Turbulence*. J.C.J. Nihoul and B.M. Jamart, Eds. Elsevier, Amsterdam, 315-335.
- Bryan, K. and Cox, M.D., 1968. A numerical model of an ocean driven by wind and differential heating: Part I. Description of the three-dimensional velocity and density fields. *J. Atmos. Sci.*, **25**, 945-967.
- Charney, J.G., 1955. The Gulf Stream as an inertial boundary layer. *Proc. Natl. Acad. Sci. U.S.A.*, **41**, 731-740.
- Chassignet, E.P., 1988. Investigation of the dynamics of the Agulhas Current system in a numerical model. Ph.D. dissertation, University of Miami, 118 pp.
- Chassignet, E.P. and Boudra, D.B., 1988. Dynamics of Agulhas Retroflection and ring formation in a numerical model. II: Energetics and ring formation. *J. Phys. Oceanogr.*, **18**, 304-319.
- Chassignet, E.P., Olson, D.B., and Boudra, D.B., 1990. Motion and evolution of oceanic rings in a numerical model and in observations. *J. Geophys. Res.*, (in press).
- Cox, M. D., 1987. Isopycnal diffusion in a z-coordinate ocean model. Unpublished manuscript. *Ocean modeling*. June.
- Darbyshire, J., 1972. The effect of bottom topography on the Agulhas Current. *Rev. Pure Appl. Geophys.*, **101**, 208-220.
- De Ruijter, W.P.M., 1982. Asymptotic analysis of the Agulhas and Brazil Current system. *J. Phys. Oceanogr.*, **12**, 361-373.
- De Ruijter, W.P.M. and Boudra, D.B., 1985. The wind-driven circulation of the South Atlantic-Indian Ocean. I: Experiments in a one-layer model. *Deep-Sea Res.*, **32**, 557-574.
- De Szoek, R.A., 1975. Some effects of bottom topography on baroclinic stability. *J. Marine Res.*, **33**, 92-122.
- Eady, E. T., 1949. Long waves and cyclone waves. *Tellus*, **1**, 33-52.
- Fine, R.A., Warner, M.J., and Weiss, R.F., 1988. Water mass modification at the Agulhas Retroflection: chlorofluoromethane studies. *Deep-Sea Res.*, **35**, 311-332.

- Gordon, A.L., 1985. Indian-Atlantic transfer of thermocline water at the Agulhas Retroflection. *Science*, **227**, 1030-1033.
- Gordon, A.L., 1986. Interocean exchange of thermocline water. *J. Geophys. Res.*, **73**, 531-534.
- Gordon, A.L., and Haxby, W., 1990. Agulhas eddies invade the South Atlantic - Evidence from Geosat altimeter and shipboard CTD. *J. Geophys. Res.*, **95**, 3117-3125.
- Harris, T.F.W., and Van Foreest, D. 1978. The Agulhas Current in March 1969. *Deep-Sea Res.*, **25**, 549-561.
- Harris, T.F.W., Legeckis, R. and Van Foreest, D., 1978. Satellite infra-red images in the Agulhas Current system. *Deep-Sea Res.*, **25**, 543-548.
- Hellerman, S. and Rosenstein, M., 1983. Normal monthly wind stress over the world ocean with error estimates. *J. Phys. Oceanogr.*, **13**, 1093-1104.
- Holland, W. R. and Lin, L.B., 1975. On the generation of mesoscale eddies and their contribution to the oceanic general circulation. I. A preliminary numerical experiment. *J. Phys. Oceanogr.*, **5**, 642-657.
- Holland, W. R. and Lin L.B., 1975. On the generation of mesoscale eddies and their contribution to the oceanic general circulation. II. A parameter study. *J. Phys. Oceanogr.*, **5**, 658-669.
- Holland, W. R., 1978. The role of mesoscale eddies in the general circulation of the ocean—numerical experiments using a wind-driven quasi-geostrophic model. *J. Phys. Oceanogr.*, **8**, 363-392.
- Holland, W. R. and Schmitz, W.J., Jr., 1985. Zonal penetration scale of model midlatitude jets. *J. Phys. Oceanogr.*, **15**, 1859-1875.
- Huang, R. X., 1986. Numerical simulation of wind-driven circulation in a subtropical/subpolar basin. *J. Phys. Oceanogr.*, **16**, 1636-1650.
- Hurlburt, H.E., and Thompson, J.D., 1980. A numerical study of Loop Current intrusions and eddy shedding. *J. Phys. Oceanogr.*, **10**, 1611-1651.
- Lighthill, M.J., 1969. Dynamic response of the Indian Ocean to onset of the Southwest Monsoon. *Phil. Trans. Roy. Soc. London*, **265**, 45-92.

- Lutjeharms, J.R.E., 1981. Spatial scales and intensities of circulations of the ocean areas adjacent to South Africa. *Deep Sea Res.*, **28A**, 1289-1302.
- Lutjeharms, J.R.E. and van Ballegooyen, R.C., 1984. Topographic control in the Agulhas Current System. *Deep-Sea Res.*, **31**, 1321-1337.
- Lutjeharms, J.R.E. and Gordon, A.L., 1987. Shedding of an Agulhas ring observed at sea. *Nature*, **325**, 138-140.
- Moore, D. W., 1963. Rossby waves in ocean circulation. *Deep-Sea Res.*, **10**, 735-748.
- Moore, D.W. and Niiler, P.P., 1974. A two-layer model for the separation of inertial boundary currents. *J. Mar. Res.*, **32**, 457-484.
- Nof, D., 1983. On the migration of isolated eddies with application to Gulf Stream rings. *J. Mar. Res.*, **41**, 399-425.
- Olson, D.B. and Evans, R.H., 1986. Rings of the Agulhas. *Deep-Sea Res.*, **33**, 27-42.
- Olson, D.B., Fine, R.A., and Gordon, A.L., 1988. Convective modifications of water masses in the Agulhas. *Deep-Sea Res.*, (accepted).
- Ou, H.W. and de Ruijter, W.P.M., 1986: Separation of an inertial boundary current from a curved coastline. *J. Phys. Oceanogr.*, **16**, 280-289.
- Parsons, A.T., 1969. A two-layer model of Gulf Stream separation. *J. Fluid Mech.*, **39**, 511-528.
- Pedlosky, Joseph, 1979. *Geophysical Fluid Dynamics*. Springer-Verlag. New York. 624 pp.
- Redi, M. H., 1982. Oceanic isopycnal mixing by coordinate rotation. *J. Phys. Oceanogr.*, **12**, 1154-1158.
- Richardson, P.L., 1983. Eddy kinetic energy in the North Atlantic from surface drifters. *J. Geophys. Res.*, **88**, 4355-4367.
- Sadourny, R., 1975. The dynamics of finite-difference models of the shallow water equations. *J. Atmos. Sci.*, **32**, 680-689.
- Schmitz, W.J. Jr., 1984. Abyssal eddy kinetic energy in the North Atlantic. *J. Mar. Res.*, **38**, 111-133.

- Thompson, J.D. and Schmitz, W.J. Jr., 1989. A limited-area model of the Gulf Stream: design, initial experiments, and model-data intercomparison. *J. Phys. Oceanogr.*, 19, 791-814.
- Veronis, G., 1973. Model of world ocean circulation: I. Wind-driven, two layer. *J. Mar. Res.*, 31, 228-288.
- Walker, N.D., and Mey, R.D., 1988. Ocean/atmosphere heat fluxes of the Agulhas Retroflection region. *J. Geophys. Res.*, (in press).
- Zalesak, S.T., 1979: Fully multi-dimensional flux-corrected transport algorithm for fluids. *J. Computat. Phys.*, 31, 335-362.

VITA

Kevin A. Maillet was born in Worcester, Massachusetts [REDACTED]. He grew up in nearby Auburn, Massachusetts where he attended Randall Elementary School and graduated from Auburn High School in May, 1983. He entered The College of the Holy Cross in Worcester, Massachusetts where he received a B.A. in physics in May, 1987.

In August 1987, he entered the University of Miami Rosenstiel School of Marine and Atmospheric Science where he was granted the Master of Science degree in Physical Oceanography in December, 1990.

Permanent address: [REDACTED]